CONFIDENTIAL

Copy 386

RM A55E31

NACA RM A55E31

NACA

CASE FILE COPY

RESEARCH MEMORANDUM

INVESTIGATION OF SOME WAKE VORTEX CHARACTERISTICS OF AN INCLINED OGIVE-CYLINDER BODY AT MACH NUMBER 1.98

By Leland H. Jorgensen and Edward W. Perkins

Ames Aeronautical Laboratory
Moffett Field, Calif.

CLASSIFICATION CHANGED TO UNCLASSIFIED

AUTHORITY: NACA RESEARCH ABSTRACT NO. 118

EFFECTIVE DATE: JULY 26, 1957 WHL

CLASSIFIED DOCUMENT

This material contains information affecting the National Defense of the United States within the meaning of the espionage laws, Title 18, U.S.C., Secs. 793 and 794, the transmission or revelation of which in any manner to an unauthorized person is prohibited by law.

NATIONAL ADVISORY COMMITTEE FOR AERONAUTICS

WASHINGTON

August 23, 1955

CONFIDENTIAL

NATIONAL ADVISORY COMMITTEE FOR AERONAUTICS

RESEARCH MEMORANDUM

INVESTIGATION OF SOME WAKE VORTEX CHARACTERISTICS OF AN INCLINED OGIVE-CYLINDER BODY AT MACH NUMBER 1.98

By Leland H. Jorgensen and Edward W. Perkins

SUMMARY

For an inclined body of revolution at a free-stream Mach number of 1.98, pitot-pressure distributions in the flow field, pressure distributions over the body, and downwash distributions through the shed vortices have been measured. The body consisted of a fineness-ratio-3, circular-arc, ogival nose tangent to a cylindrical afterbody 7.3 diameters long. The free-stream Reynolds numbers, based on body diameter, were 0.15×10^6 and 0.44×10^6, and the angle-of-attack range was from 5° to 20°. Pressure distributions on the body surface have been used in conjunction with flow-field contour plots of constant pitot pressure to determine the approximate locations at which the vortices left the body surface and their paths downstream.

To aid in the study of the experimental data, expressions have been written for the flow about a simple theoretical model in which the induced flow field in any crossflow plane along the cylindrical afterbody is represented by the incompressible steady potential flow around a cylinder in the presence of two symmetrical vortices of equal strength. By the use of velocity and vortex strength formulae resulting from consideration of this theoretical model, vortex paths which agree well with the experimental paths have been computed. However, in computing these paths, starting vortex positions and strengths determined from experiment were used, since there is no reliable theoretical method for determining these starting conditions.

Comparisons of theoretical and experimental downwash angle distributions along a line through the vortex centers illustrate the inadequacy of the sometimes-used potential flow about a cylinder which fails to account for the presence of vortices in the flow field. Except through and between the vortex cores, the downwash can be closely computed by assuming two symmetrical potential vortices in the flow field. If the sizes of the core radii are known, the agreement of theory with experiment

both through and between the cores can be improved by the assumption of viscous rather than potential vortices in the field.

INTRODUCTION

One phase of the general problem of the interference between component parts of aircraft that has received little attention thus far is the interference effects resulting from the vortices shed from a body of revolution at large angles of attack. Wind-tunnel tests have shown that these vortices can have a large effect upon the forces developed on wing and tail surfaces. Fortunately, techniques are available for estimating the forces developed on the wing and tail surfaces provided the strengths and positions of the body vortices are known (see, e.g., ref. 1). Although, as yet, there is no rigorous theoretical method for predicting either the strengths or the positions of the vortices, certain simplified methods for estimating these characteristics can be suggested.

The purpose of this report is twofold: first, to present experimental results of flow-field characteristics about an inclined body of revolution and second, to assess the adequacy of a simplified method of estimating these characteristics. To this end an inclined body of revolution has been utilized for obtaining measurements of body pressure distributions, paths of the shed vortices, and downwash distributions through the vortex cores. Comparisons of computed vortex paths and downwash distributions are made with the results of the experimental measurements.

SYMBOLS

A	reference area, πa^2
a	radius of cylindrical portion of body
c	a constant of integration
C_N	normal-force coefficient, $\frac{N}{q_o A}$
C_{N_p}	normal-force coefficient by Tsien's potential theory
C_p	pressure coefficient, $\frac{p - p_o}{q_o}$
d	body diameter
l	body length
l_n	length of ogival nose

M_o	free-stream Mach number
N	normal force
p	local static pressure on body
p_o	free-stream static pressure
p_p	pitot pressure in body flow field (measured parallel to body axis)
p_{t_o}	free-stream total pressure
q_o	free-stream dynamic pressure
Re	free-stream Reynolds number per inch
r_*	core radius of viscous vortex
r_v	radial distance from vortex center to point y,z in crossflow plane
s	position of a point in crossflow plane, y + iz
t	time of vortex growth
v,w	induced velocities in y and z directions, respectively (see sketch (a) p. 6)
V_o	free-stream velocity
V_c	crossflow velocity, $V_o \sin \alpha \approx V_o \alpha$
V_r	vortex velocity in crossflow plane, $\sqrt{v^2 + w^2}$
x,y,z	Cartesian coordinates of point in space, origin at nose vertex, x axis coincident with body axis, z axis perpendicular to x axis in pitch plane. (See sketch (a) p. 6)
x,r,θ	cylindrical coordinates of point in space (origin at nose vertex, x axis coincident with body axis, and $\theta = 0^o$ in crossflow plane on windward side)
α	angle of attack
Γ	circulation strength

ϵ local flow (downwash) angle with respect to free-stream direction, $\alpha - \frac{w}{V_o}$

ζ position of vortex center in crossflow plane, $\xi + i\eta$

μ,ξ,η Cartesian coordinates of vortex filament position (referred to body axis with origin at nose)

ν kinematic viscosity of air

ρ free-stream air density

σ sidewash angle with respect to free-stream direction, $\frac{v}{V_o}$

φ potential function in crossflow plane

ψ stream function in crossflow plane

Subscripts

x conditions at "x" distance from nose vertex

$n=1,2,3,4$ identifies real and image vortices (see sketch (b) p. 7)

EXPERIMENTAL CONSIDERATIONS

Apparatus

The experimental investigation was conducted in the Ames 1- by 3-foot supersonic wind tunnel No. 1. This tunnel is a closed-circuit variable-pressure tunnel in which the Reynolds number is changed by varying the total pressure within the approximate limits of one-fifth of an atmosphere to two atmospheres. Mach numbers between 1.2 and 2.5 are obtained by adjustment of the upper and lower flexible steel plates of the nozzle.

The model tested had a fineness-ratio-3, circular-arc, ogival nose tangent to a cylindrical afterbody 7.3 diameters long. A single row of 23 orifices extended longitudinally over both nose and afterbody. The model, which was constructed of steel, was sting supported from the rear and could be rotated 360° about its longitudinal axis by a mechanism operated from outside the tunnel. Pertinent model dimensions are shown in figure 1(a).

Sketches of the pitot-survey rake and survey cone which were used to measure total pressures and local stream angles, respectively, are shown in figures 1(b) and 1(c). Photographs of the model and survey cone apparatus are presented in figures 1(d) and 1(e). The pitot-survey rake could be mounted on the body at various model length positions and could be rotated with the model about the model longitudinal axis. The survey cone was supported on a movable strut projecting from the steel side plate which replaced a tunnel window (fig. 1(d)). The cone could be positioned laterally in the tunnel to within ±0.01 inch by the use of a hand crank and lateral position scale (fig. 1(e)). In addition, the cone could be pitched about the lateral strut axis which passed midway between the top and bottom (downwash) orifices of the cone. The pitch angle could be set to within ±0.05°.

Pressure leads from the body, pitot rake, and survey cone were connected to a liquid manometer system. The pressures were photographically recorded.

Tests and Results

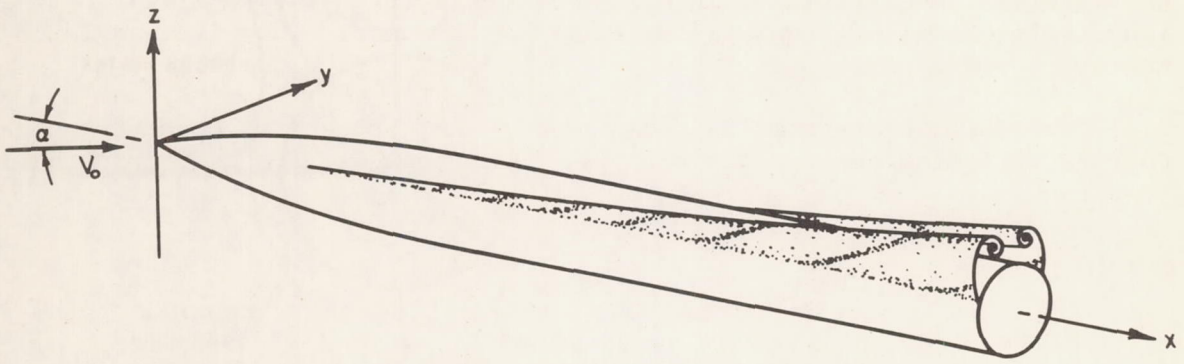
All data were obtained for a free-stream Mach number of 1.98. The model was tested at angles of attack of 5°, 10°, 15°, and 20° for a free-stream Reynolds number of 0.39×10^6 per inch and at an angle of attack of 15° for a Reynolds number of 0.13×10^6 per inch (Reynolds numbers of 0.44×10^6 and 0.15×10^6 based on body diameter). Circumferential pressure distributions were obtained by rotating the model through the desired range of circumferential angle (θ). At various model length stations (x/d) pitot-pressure distributions of the flow field were obtained also by rotating the model about its longitudinal axis.

Downwash angle measurements were made along horizontal lines perpendicular to the model pitch plane and passing approximately through the vortex centers. The downwash angle surveys were made by the null-cone method in which the cone is pitched until the pressures measured at the top and bottom cone orifices indicate that the axis of the cone is alined with the local stream. The repeatability of the measurements was checked by making random reruns. Except at positions very close to the vortex centers where the induced velocity gradients were large, it was found that the downwash angles generally could be repeated to within ±0.2°.

All of the pressure data for the model surface were reduced to coefficient form and are tabulated in reference 2 and plotted in figures 2 through 6. The pitot-pressure data for the model flow field were reduced to the form of the ratio of local pitot pressure to free-stream total pressure, p_p/p_{t_o}. Contour plots of constant values of p_p/p_{t_o} are presented in figures 2 through 6. Downwash angles, measured in degrees with reference to the free-stream flow direction, are listed in tables I and II.

THEORETICAL CONSIDERATIONS

Calculation of the interference effects resulting from the vortices shed from a lifting body depends to a large extent upon an understanding of the manner in which the vorticity is discharged from the body and upon a satisfactory representation of the induced flow downstream of the body nose. From visual flow studies (e.g., ref. 3) it is known that the physical flow field for moderate angles of attack is approximately as indicated in sketch (a). The vortex formation for the body is somewhat similar to



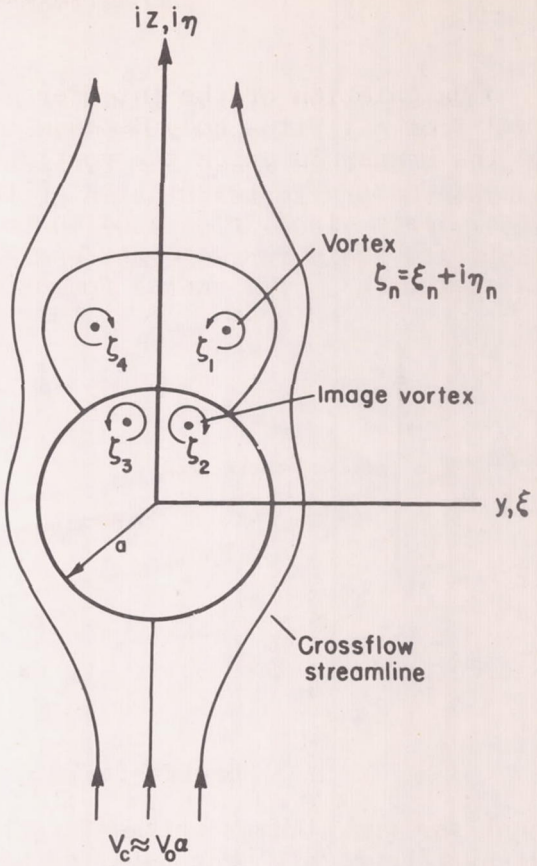
Sketch (a).- Assumed flow field.

that for the slender triangular plan-form wing considered by Brown and Michael (ref. 4). For both the body and the wing two spiral vortex sheets are produced, with flow separation occurring on the sides of the inclined body and on the leading edges of the wing. The sheets roll up to form two regions of concentrated vorticity. The large flow angles associated with these regions of vorticity are responsible for interference effects. The complex nature of the actual flow precludes an exact representation of the three-dimensional flow field; hence, a simplified model of the real flow must be chosen for study. In this section of the report expressions for the flow about a simple theoretical model are presented.

Theoretical Model and Basic Formulae for Potential and Velocities in the Flow Field

The assumption of slender-body theory that the flow is independent of Mach number is made. It is assumed that the induced flow field in any crossflow plane along the cylindrical afterbody can be adequately represented as the steady two-dimensional, incompressible potential flow around a circular cylinder in the presence of two symmetrical vortices of

of equal strength (sketch (b)) All of the vorticity is considered to be concentrated in the two external vortices, the effects of the feeding vortex sheets being omitted. In addition, it is assumed that the vortices need be considered only at positions downstream of the nose-cylinder junction. The boundary condition of tangential flow at the body surface is satisfied by placing image vortices within the body at the appropriate positions.



Sketch (b).- Approximate flow field representation in a crossflow plane.

The complex potential equation for the crossflow (sketch (b)) is

$$\varphi + i\psi = -V_c i\left(s - \frac{a^2}{s}\right) - \frac{i\Gamma}{2\pi}\ln\frac{(s - \zeta_1)(s - \zeta_3)}{(s - \zeta_2)(s - \zeta_4)} \qquad (1)$$

where $|\Gamma|$ is the magnitude of the strength of each vortex; $s = y + iz$ is the position of a point in the field; and ζ_1, ζ_2, ζ_3, and ζ_4 are the positions of the real and image vortices, with $\zeta_n = \xi_n + i\eta_n$. Resulting expressions from which the velocities induced at any position (y,z) can be calculated are as follows:

$$w = V_c\left[1 + \frac{a^2(y^2 - z^2)}{(y^2 + z^2)^2}\right] - \frac{\Gamma}{2\pi}\sum_{n=1}^{n=4}(-1)^n\left[\frac{y - \xi_n}{(z - \eta_n)^2 + (y - \xi_n)^2}\right] \qquad (2)$$

$$v = -\frac{2V_c a^2 yz}{(y^2 + z^2)^2} + \frac{\Gamma}{2\pi}\sum_{n=1}^{n=4}(-1)^n\left[\frac{z - \eta_n}{(z - \eta_n)^2 + (y - \xi_n)^2}\right] \qquad (3)$$

where

$$V_c \approx V_o\alpha$$

$$\xi_4 = -\xi_1$$

$$\xi_3 = -\xi_2 = -\frac{a^2\xi_1}{\xi_1^2 + \eta_1^2}$$

$$\eta_4 = \eta_1$$

and

$$\eta_3 = \eta_2 = \frac{a^2\eta_1}{\xi_1^2 + \eta_1^2}$$

Downwash and sidewash angles (with respect to the free-stream direction) are then given approximately by $\epsilon \approx \alpha - (w/V_o)$ and $\sigma \approx (v/V_o)$.

Velocity Relationships With Viscous Vortices

Because of the effects of viscosity, downwash and sidewash distributions computed by equations (2) and (3) cannot be expected to agree closely with experiment near to and at the vortex centers. It is likely, however, that the agreement of theory with experiment can be improved by substituting theoretical viscous vortices for potential vortices in the flow field. For a single isolated viscous vortex it has been shown (ref. 5, p. 592) that the velocity varies according to the expression,

$$V_r = \frac{\Gamma}{2\pi r_v}\left(1 - e^{-r_v^2/4\nu t}\right) \qquad (4)$$

where

$$V_r = \sqrt{v^2 + w^2}$$

$$r_v = \sqrt{(z - \eta)^2 + (y - \xi)^2}$$

ν = kinematic viscosity

and

$$t = \text{time of vortex growth}$$

What is assumed to be a viscous vortex is, in essence, a vortex having a "solid" core with potential outer flow joined by a transition region. In this transition region, at some radial distance, r_*, from the vortex center the velocity reaches a maximum. Using equation (4) it can be shown (see, e.g., ref. 6) that r_* can be expressed as a simple function of time, t, by

$$r_* = 2.24(\nu t)^{1/2} \tag{5}$$

In this report, r_* is assumed to be the core radius of the viscous vortex.

For the complete flow field, if it is assumed that both the real and image vortices have core radii which are equal in magnitude, then approximate formulae for induced velocities in the field can be written as follows:

$$w = V_c\left[1 + \frac{a^2(y^2 - z^2)}{(y^2 + z^2)^2}\right] - \frac{\Gamma}{2\pi}\sum_{n=1}^{n=4}(-1)^n\left[\frac{y - \xi_n}{(z - \eta_n)^2 + (y - \xi_n)^2}\right](1 - e^B) \tag{6}$$

$$v = -\frac{2V_c a^2 yz}{(y^2 + z^2)^2} + \frac{\Gamma}{2\pi}\sum_{n=1}^{n=4}(-1)^n\left[\frac{z - \eta_n}{(z - \eta_n)^2 + (y - \xi_n)^2}\right](1 - e^B) \tag{7}$$

where

$$B = -1.254(1/r_*)^2\left[(z - \eta_n)^2 + (y - \xi_n)^2\right]$$

It is of note that these formulae, due to the linear superposition of a viscous onto a potential flow system, are not mathematically rigorous and do not satisfy the body boundary condition of zero normal velocity for all values of θ in the crossflow plane. However, at least for positions through and in the vicinity of the vortices, their use can be justified on the basis of good agreement between computed and experimental downwash distributions (discussed later in the report).

Vortex Strengths, Origins, and Paths

Vortex strengths.- For a theoretical model in which two symmetrical vortices originate on and remain in the presence of an infinitely long circular cylinder, the strength of the vortices at a given station, x, can be related to the normal force on the portion of the cylinder between the origin of the vortices and station x by the Kutta-Joukowsky law (see, e.g., ref. 7). Thus,

$$(N_{cyl})_x = \rho \Gamma_x V_o (2\xi_1 - 2\xi_2)_x \tag{8}$$

For the considered theoretical model, which includes a slender ogival nose with a pair of symmetrical vortices originating on the cylinder or at the nose-cylinder junction, the total normal force at a given x station can be approximated by

$$N_x = (N_{cyl})_x + N_{nose} = \rho \Gamma_x V_o (2\xi_1 - 2\xi_2)_x + 2\alpha q_o A \tag{9}$$

Thus,

$$\left(\frac{\Gamma}{V_o}\right)_x = \frac{\left(C_{N_x} - 2\alpha\right) A}{4(\xi_1 - \xi_2)_x} \tag{10}$$

where C_{N_x} is the coefficient of the total normal force developed from the nose vertex to the body-length station considered. The normal-force coefficient for the nose portion of the body is the slender-body result of $C_N = 2\alpha$. For this theoretical model any so-called "lift carry-over" from the nose onto the cylinder is neglected. The lift on the cylinder is considered to be only that resulting from the motion of the vortices relative to the cylinder (the slender-body value of lift being zero over the cylinder). Experimental data (ref. 2), however, indicate that, even for the body at low angles of attack (of the order of 5°), there is a moderate amount of lift carry-over from the nose onto the cylinder. Studies of these data have shown that this lift carry-over can be accounted for, at least in part, by the use of Tsien's potential theory (ref. 8) in preference to slender-body theory. Hence, a preferred hybrid expression relating vortex strength and position to normal-force coefficient can be written as

$$\left(\frac{\Gamma}{V_o}\right)_x = \frac{\left(C_N - C_{N_p}\right)_x A}{4(\xi_1 - \xi_2)_x} \tag{11}$$

where C_{N_p} is the normal-force coefficient computed by Tsien's theory. The use of equation (10) or (11) is, of course, tantamount to assuming that only the so-called viscous crossflow component of the body normal force contributes to the vortex strength.

Vortex origins.- No theoretical procedure is known for predicting the positions of the origins of the vortices (that is, the positions at which the vortices leave the body surface). Qualitatively it is known that as the angle of attack of the body is increased, the boundary layer first begins to thicken on the downstream lee side. This is followed by separation of the boundary layer and formation of two regions of concentrated vorticity in the wake on the lee side of the body. Moore (ref. 9) has studied the three-dimensional boundary-layer flow on inclined cones and has found that on the lee side of the cone, unique solutions to the classical boundary-layer-flow equations are limited to small angles of attack. Beyond a certain critical angle of attack, dependent on Mach number and cone angle, the boundary layer cannot remain thin. The critical angle of attack is of the same order as the semivertex angle of the cone. Moore presumes that for angles of attack in excess of this critical value, the flat vortex bubbles which have formed on the lee side of the cone must be in the process of forming a symmetric pair of strong vortices. Similar considerations probably apply for the flow about inclined bodies other than cones. Consideration of pressure distributions along streamlines on an inclined cylinder indicate that, because of the adverse pressure gradient, there is a tendency toward separation and formation of a vortex bubble even at very low angles of attack. However, as yet there is no method for calculating the position on an inclined body at which coalescence of the vorticity has progressed to such a degree that a symmetric pair of steady vortices are formed. Hence, experimental measurements (some of which are presented in this report) must be relied upon entirely.

Vortex paths.- With the aid of equations (2) and (3) the paths of the vortex centers can be computed by stepwise procedures if the origins and strengths of the vortices are known. For example, if a vortex position (ξ,η) and strength (Γ/V_o) are known, values of w/V_o and v/V_o induced at the filament of the vortex can be computed by equations (2) and (3).[1] If in a given time interval Δt the vortex filament can be considered to move (with respect to the body) an axial distance $\Delta\mu \approx V_o\Delta t$, a vertical distance $\Delta\eta = w\Delta t$, and a lateral distance $\Delta\xi = v\Delta t$; then,

$$\Delta\eta \approx \Delta\mu(w/V_o) \tag{12}$$

and

$$\Delta\xi \approx \Delta\mu(v/V_o) \tag{13}$$

[1]The more complex expressions, equations (6) and (7), also can be used; however, essentially the same results are obtained with equations (2) and (3).

Hence, for a small incremental distance $\Delta\mu$, a new vortex center position can be estimated by the use of equations (12) and (13). Then if the strength of the vortex is known at this new body length station and at succeeding stations, this computation process may be repeated a sufficient number of times to determine the path. If the normal-force distribution over the body is known,[2] the vortex strength at each $\Delta\mu$ interval can be estimated by equation (11). The proper spacing $\Delta\mu$ of successive stations should be, of course, checked by trial and error. For the stepwise calculations made for this investigation the experimental normal-force distributions of reference 2 have been used.

DISCUSSION

In this section of the report the pressure distribution and pitot-pressure data are used to illustrate the flow conditions on the body which lead to the formation of the vortices and to isolate the positions along the body at which the vorticity is concentrated into two well-defined vortex centers. As an aid in assessing the usefulness of the simple theoretical flow model previously outlined, comparisons of computed vortex paths and downwash distributions are made with the results of the experimental measurements.

Experimental Pressure Distributions and Vortex Positions

From a study of the pressure distributions on the surface of the body and pitot-pressure distributions in the flow field on the lee side of the body, the positions at which the body vortices originated and the paths of the vortices downstream from the origin can be determined. The body pressure distribution data and the pitot-tube survey data have been plotted in figures 2 through 6 to show constant pressure contours for each of the test conditions.[3] On the contour plots of body pressure coefficient, lines are shown to indicate the circumferential positions of minimum pressure coefficient (C_p minimum with respect to θ), the approximate flow-separation positions, and the circumferential locations of the vortex centers. The minimum pressure positions, of course, are obvious. The flow-separation and vortex-center positions will be discussed in the following paragraphs.

---

[2]If the normal-force distribution is not known from experiment it can sometimes be computed by a semiempirical method (see, e.g., ref. 2).

[3]Since the pitot-pressure tubes were always alined with the body axis and not with the local stream direction, some of the indicated loss in pitot pressure results from the large inclination of the stream relative to the axes of the tubes.

The pitot-pressure plots are very useful for determining the positions of the vortex centers. The vortex center positions, indicated in figures 3 through 6, are assumed to be at the approximate centers of the smallest closed contours of p_p/p_{t_o}. It is interesting to note that these positions, when superimposed on schlieren photographs of the flow field taken with the knife edge horizontal, coincide with the inner edges of the dark vortex regions. (See, e.g., fig. 7.)

The conditions leading to flow separation and subsequent formation of the vortices are perhaps best illustrated by typical pressure distributions along approximate streamlines on the cylindrical afterbody (fig. 4).[4] For $\alpha = 15^\circ$ and $Re = 0.39 \times 10^6$ per inch, pressure distributions along the streamlines shown in figure 4 are plotted in figure 8. Along the streamlines the pressure decreases rapidly proceeding from the windward toward the leeward side of the body. A minimum pressure is reached near the side of the body. This is followed by a rising pressure (adverse pressure gradient) and eventual flow separation. The flow separation position is assumed to coincide with the point at which the pressure then begins to decrease. Following flow separation a second minimum pressure occurs (except for streamline a) at the approximate circumferential location of the vortex center. (Although the identity of the individual streamlines is lost beyond the flow separation point, these plots have been continued by dashed lines into the separated flow region to show the influence on the pressure distributions of the secondary flow associated with the vortices.)

From a study of the differences between the pressure distributions along the various streamlines coupled with a study of the pitot-pressure plots for various x/d positions, the approximate region of the origin of the vortices can be determined. For instance, for the pressure distribution along the streamline labeled "a" there is no clear indication of flow separation, nor is there any second minimum pressure that has been associated with the location of the vortex core. However, along the streamline labeled "b" there is an indication of a vortex forming at an x/d position of about 4. Since the pitot survey data (fig. 4) show that the vortices are clearly developed at $x/d = 5.8$, it is reasonable to assume that the vortices originated at about 4 or 5 diameters from the nose. From similar studies of the data for the other angles of attack (5°, 10°, and 20°) additional information concerning the approximate origin of the vortices has been determined. In figure 9 the approximate length positions at which the effects of the vortices were first discernible in the pressure distributions are plotted as a function of angle of attack.

A considerable effect of Reynolds number upon the flow about the inclined body of this investigation was previously reported in reference 2.

[4]These streamlines, which were derived simply from consideration of incompressible potential flow over an inclined circular cylinder (with no vortices considered), are defined by $\theta = 2 \tan^{-1}(ce^{4\alpha x/d})$.

The changes in the pressure distribution and flow-separation characteristics at $\alpha = 15^{\circ}$ for an increase in Reynolds number from 0.13×10^6 to 0.39×10^6 per inch can be seen by comparing figures 5 and 4. Although there is a significant effect upon the pressure distributions, comparison of corresponding pitot-pressure plots reveal only a small effect upon the vortex positions. For the lower Reynolds number tests the positions of the vortex centers at $x/d = 5.8$ were approximately 0.1 body radius farther from the body surface and about 5° closer to the vertical plane of symmetry than for the higher Reynolds number. At the base of the body, $x/d = 10.3$, the locations of the vortices were practically identical for both Reynolds numbers.

Vortex Strengths Computed From Experiment

To provide values of vortex strength to aid in assessing the methods of computing the vortex paths and the downwash distributions, the strengths of the vortices at various body length positions have been computed by equations (10) and (11). They are presented nondimensionally in figure 10 as $\Gamma/2\pi a V_o$ as a function of x/d. The calculations have been made using the experimental normal-force distributions of reference 2 with both measured and computed vortex positions taken at various body length stations. The measured vortex positions were obtained from figures 3 through 6. Where the vortices are shown to be slightly asymmetric, average values of the positions have been used. The strengths obtained using computed vortex positions (discussed later) result from application of the stepwise path calculation method previously outlined.

In general, the strengths of the vortices would be expected to increase with distance downstream. It is believed that the small decreases in some of the computed vortex strengths with distance downstream are a result of approximations in the methods used and do not actually exist.

Comparisons of Theoretical and Experimental Vortex Paths

Theoretical and experimental vortex path positions are compared in figure 11. The experimental positions were taken from the pitot-pressure contour plots (figs. 3 through 6). The theoretical path positions were computed by the stepwise method (previously outlined) in which the vortex strength is computed by equation (11) and varies with distance x downstream (as shown in fig. 10). In addition, calculations were made by the stepwise procedure but with the vortex strength held constant over the path length and given by $\Gamma/V_o = 4a\alpha$, an assumed relation to be mentioned later. The Föppl equilibrium positions for vortices in the crossflow plane of a two-dimensional cylinder (ref. 5, p. 223) are also presented in figure 11 merely for reference. All stepwise path calculations were started at the most forward body length positions at which pitot-pressure surveys revealed the presence of well-defined vortices. Incremental

length spacings ($\Delta\mu$'s) of 25 percent of the body radius were used, although $\Delta\mu$'s of 50 percent of the radius were found to be satisfactory. For the stepwise method in which Γ/V_o varies with x, the initial vortex strengths at the starting positions were assumed to be the same as those computed using the measured vortex positions of this investigation and the normal-force distributions in figure 8 of reference 2. In general, the paths computed by this method are in very good agreement with experiment. However, for $\alpha = 15^\circ$ and Re = 0.39×10^6 per inch, it appears that the initial vortex strength calculated from experiment is too large, and as a result the computed vortex position initially moves too far in the ξ direction and not far enough in the η direction (as shown in the end view of fig. 11(b)). However, with increase in distance downstream the strength computed by the stepwise method decreases at a sufficient rate (see fig. 10) so that the computed path agrees reasonably well with experiment even though the initial vortex strength seems much too large. For the other test conditions the initial strengths seem to be about right, and the agreement between the computed and measured path positions is very good.

Further investigation into the computation of the paths revealed that the vortex strengths only had to be approximated in order to compute the paths reasonably well. In fact, it was found that the strengths could be assumed to remain constant over the path lengths for each angle of attack. For example, at all α's the paths were satisfactorily computed (see fig. 11) by assuming the strengths to be given by $\Gamma/V_o = 4a\alpha$, an expression which was merely chosen to give the correct value of strength (according to fig. 10) for $\alpha = 10^\circ$ but which underestimates the strengths for 15° and 20°.

It is interesting to note that, although there was a considerable effect on the body loading at 15° angle of attack due to change in Reynolds number from 0.13×10^6 to 0.39×10^6 per inch, there was only a small effect on the vortex positions, and the vortex paths for both Reynolds numbers can be computed reasonably well. Although there may be larger effects on the paths due to greater changes in Reynolds number, the data of this investigation indicate that the effect of Reynolds number on the paths need be considered only in determining the proper starting positions. As yet, no reliable solution to the starting problem has been determined.

Comparisons of Theoretical and Experimental Downwash Distributions Through the Body Vortices

Comparisons of theoretical and experimental downwash angle distributions along a line through the body vortices at various length stations and at angles of attack of 10°, 15°, and 20° are presented in figure 12. (Since the downwash surveys were made along horizontal lines passing just a little above or below the vortex centers, the z/a survey locations

are not quite equal to the η/a vortex center locations shown in figure 12.) For the test conditions of this investigation the effect on the downwash distributions due to change in Reynolds number was small. Typical comparisons of downwash distributions for Reynolds numbers of 0.13×10^6 per inch and 0.39×10^6 per inch are shown in figure 13. Since the Reynolds number effects were small, only data for one Reynolds number (Re = 0.39×10^6 per inch) have been used for the comparisons with theory.

The comparisons of theory with experiment (fig. 12) show that the downwash distributions computed using only the potential flow around the cylinder with $\Gamma/V_o = 0$ are completely erroneous; whereas, the distributions computed with the inclusion of a symmetrical pair of potential vortices (and images) superimposed in the flow field agree well with experiment except between and close to the vortex centers. The downwash distributions which include the effects of potential vortices (see eq. (2)) were computed with values of vortex strength taken from figure 10 (eq. (11)) and also from the assumed relation $\Gamma/V_o = 4a\alpha$. Except for $\alpha = 20^\circ$ at x/d's greater than 6.7 where the distributions computed with $\Gamma/V_o = 4a\alpha$ differ appreciably from experiment, about the same agreement between theory and experiment is obtained with either method of estimating the strength. This, of course, is not surprising since the values of vortex strength from the assumed formula and from experiment only differ markedly for $\alpha = 20^\circ$.

Although the distributions computed with potential vortices superimposed in the flow field agree well with experiment at lateral positions (y's) greater than about 1.5 body radii from the vertical axis of symmetry, the agreement near the vortex cores is poor. Close to and through the vortex cores the experimental distributions can be more nearly duplicated by the assumption of viscous instead of potential flow vortices (see eq. (6)). This is demonstrated clearly in figure 12(b) for $\alpha = 15^\circ$ at $x/d = 8.8$. For the computed distributions in figure 12(b) all of the core radii (including images) were assumed to be equal and of the same magnitude as the core radii estimated from the experimental distribution ($r_*/a = 0.28$, the y/a distance from the vortex center to the maximum negative value of ϵ). Theoretically, the size of a core radius can be considered to be a simple function of the kinematic viscosity and the time of development of the vortex (see eq. (5)). However, without a clearer understanding of the time history and viscosity of the vortices, it is difficult to make a logical estimate of the core size. For example, the product νt computed from free-stream conditions indicates that viscosity is of minor importance, since the resulting magnitude of r_* by equation (5) is negligibly small compared to the value indicated by experiment.

At $\alpha = 20^\circ$ the agreement between theory and experiment is somewhat adversely affected because of the effect of wake shock waves (see figs. 12(d), (e), (f), and (g)). These shock waves, which have been observed in previous visual studies of the wake shed from inclined

flat-nosed cylinders and pointed bodies (refs. 10 and 11), apparently are formed when the crossflow Mach number ($M_o \sin \alpha$) exceeds about 0.5. The downwash data indicate that these waves move outboard and toward the windward side of the body with increase in distance downstream.

CONCLUSIONS

A body with a fineness-ratio-3, circular-arc, ogival nose tangent to a cylindrical afterbody 7.3 diameters long has been tested in the Ames 1- by 3-foot supersonic wind tunnel No. 1 at a free-stream Mach number of 1.98. Pitot-pressure distributions in the flow field, pressure distributions over the body, and downwash measurements through the body vortices have been obtained for angles of attack to 20°. Pressure distributions on the body surface and pitot-pressure contours in the flow field have been used to determine the approximate positions at which the vortices left the body surface and their paths downstream. An analysis of these data in conjunction with a simple theoretical flow model, which has been outlined in the report, has led to the following conclusions:

1. The paths of symmetrically shed body vortices can be computed quite accurately by the use of a simple stepwise method. However, in the application of this method, a knowledge of the body normal-force distribution and the starting positions and strengths of the vortices is required. Additional research on the problem of predicting the starting positions and strengths of the vortices is necessary.

2. Although not confirmed by detailed measurements of the flow field, it appears that the strengths of the concentrated body vortices can be estimated from the normal-force distributions and vortex positions.

3. Flow angle distributions through the body vortices computed by the potential flow about a cylinder are completely erroneous; whereas, distributions computed by assuming a pair of symmetric potential vortices (and images) superimposed in the flow field agree well with experiment, except between and through the vortex cores.

Ames Aeronautical Laboratory
National Advisory Committee for Aeronautics
Moffett Field, Calif., May 31, 1955

REFERENCES

1. Nielsen, Jack N., Kaattari, George E., and Anastasio, Robert F.: A Method for Calculating the Lift and Center of Pressure of Wing-Body-Tail Combinations at Subsonic, Transonic, and Supersonic Speeds. NACA RM A53G08, 1953.

2. Perkins, Edward W., and Jorgensen, Leland H.: Comparison of Experimental and Theoretical Normal-Force Distributions (Including Reynolds Number Effects) On An Ogive-Cylinder Body at Mach Number 1.98. NACA RM A54H23, 1954.

3. Gowen, Forrest E., and Perkins, Edward W.: A Study of the Effects of Body Shape on the Vortex Wakes of Inclined Bodies at a Mach Number of 2. NACA RM A53I17, 1953.

4. Brown, C. E., and Michael, W. H., Jr.: Effect of Leading-Edge Separation on the Lift of a Delta Wing. Jour. Aero. Sci., vol. 21, no. 10, Oct. 1954, pp. 690-694.

5. Lamb, Sir Horace: Hydrodynamics. Sixth Ed., Dover Pub., 1945.

6. Roshko, Anatol: On the Development of Turbulent Wakes from Vortex Streets. NACA TN 2913, 1953.

7. Lagerstrom, P. A., and Graham, M. E.: Aerodynamic Interference in Supersonic Missiles. Douglas Aircraft, Inc., Santa Monica. Rep. No. SM-13743, July 1950.

8. Tsien, Hsue-Shen: Supersonic Flow Over an Inclined Body of Revolution. Jour. Aero. Sci., vol. 5, no. 12, Oct. 1938, pp. 480-483.

9. Moore, Franklin K.: Laminar Boundary Layer on Cone in Supersonic Flow at Large Angle of Attack. NACA TN 2844, 1952.

10. Hall, I. M.: Experiments on Supersonic Flow Over Flat-Nosed Circular Cylinders at Yaw. The Philosophical Magazine, Mar. 1954. Ser. 7, vol. 45, pp. 333-343.

11. Seiff, Alvin, Sandahl, Carl, Chapman, Dean R., Perkins, Edward W., and Gowen, Forrest E.: Aerodynamic Characteristics of Bodies at Supersonic Speeds - A Collection of Three Papers. NACA RM A51J25, 1951.

TABLE I.- EXPERIMENTAL DOWNWASH ANGLES MEASURED THROUGH MODEL VORTICES AT MACH NUMBER 1.98, Re = 0.39×10^6 PER INCH

(a) $\alpha = 10^\circ$; x/d = 10.3; z/a = 1.28		(b) $\alpha = 15^\circ$; x/d = 8.8; z/a = 1.56		(c) $\alpha = 15^\circ$; x/d = 10.2; z/a = 1.82		(d) $\alpha = 20^\circ$; x/d = 5.1; z/a = 1.29				(e) $\alpha = 20^\circ$; x/d = 6.7; z/a = 1.78				(f) $\alpha = 20^\circ$; x/d = 8.5; z/a = 2.15		(g) $\alpha = 20^\circ$; x/d = 10.2; z/a = 1.97	
								Check run				Check run					
$\frac{y}{a}$	ϵ, deg	$\frac{y}{a}$	ϵ, deg	$\frac{y}{a}$	ϵ, deg	$\frac{y}{a}$	ϵ, deg	y/a	ϵ, deg	$\frac{y}{a}$	ϵ, deg	y/a	ϵ, deg	$\frac{y}{a}$	ϵ, deg	$\frac{y}{a}$	ϵ, deg
-6.40	-0.40	-6.40	-1.05	-6.40	-0.95	-6.75	0.45	-6.75	0.40	-6.75	-0.45	-6.75	-0.40	-6.75	-1.25	-6.40	-2.10
-6.04	-.45	-5.67	-1.45	-5.70	-1.05	-6.40	.30	-6.40	.20	-6.04	-.90	-6.40	-.63	-6.40	-1.65	-5.67	-1.75
-5.67	-.45	-4.98	-1.27	-4.98	-1.40	-6.04	.10	-6.04	-.05	-5.67	-1.25	-6.04	-.90	-5.67	-2.20	-4.98	-2.35
-5.33	-.60	-4.27	-1.65	-4.27	-1.75	-5.67	-.15	-5.67	-.25	-5.33	-1.55	-5.67	-1.20	-4.98	-3.00	-4.27	-3.18
-4.98	-.60	-3.56	-2.25	-3.56	-2.40	-5.33	-.40	-5.33	-.45	-4.98	-2.00	-5.33	-1.50	-4.27	-2.30	-3.56	-4.35
-4.62	-.65	-2.84	-2.70	-2.85	-2.85	-4.98	-.75	-4.98	-.82	-4.62	-2.44	-4.98	-1.95	-3.56	-3.55	-2.84	-6.15
-4.27	-.80	-2.49	-3.75	-2.49	-3.80	-4.62	-1.20	-4.62	-1.30	-4.27	-3.04	-4.62	-2.40	-2.84	-5.17	-2.49	-7.35
-3.91	-1.00	-2.13	-4.70	-2.13	-4.55	-4.27	-1.60	-4.27	-1.75	-3.91	-3.67	-4.27	-2.94	-2.49	-6.45	-1.78	-10.75
-3.56	-1.10	-1.78	-6.20	-1.78	-6.00	-3.91	-2.20	-3.91	-2.30	-3.56	-4.36	-3.91	-3.57	-2.13	-8.20	-1.42	-12.85
-3.20	-1.30	-1.42	-8.40	-1.42	-8.56	-3.56	-3.00	-3.56	-3.00	-3.20	-3.25	-3.56	-4.31	-1.78	-10.75	-1.24	-11.35
-2.84	-1.50	-1.24	-11.65	-1.24	-10.77	-3.20	-3.85	-3.20	-3.90	-2.49	-4.80	-2.84	-3.97	-1.60	-12.39	-1.07	-4.65
-2.49	-1.80	-1.07	-15.50	-1.07	-12.13	-2.49	-6.45	-2.49	-6.30	-2.13	-6.73	-2.49	-4.90	-1.42	-14.38	-.89	1.25
-2.13	-2.10	-.89	-7.50	-.89	-7.20	-2.13	-8.35	-.71	2.40	-1.78	-9.40	-2.13	-6.63	-1.24	-14.92	-.71	11.50
-1.78	-2.70	-.71	10.95	-.80	-1.65	-1.73	-7.30	-.53	14.80	-1.42	-13.26	-1.78	-9.25	-1.07	-12.76	-.53	27.35
-1.42	-3.45	-.53	18.40	-.71	6.04	-1.42	-7.00	-.36	19.50	-1.24	-14.57	-1.42	-13.41	-.89	-7.75	.53	29.50
-1.24	-4.05	-.36	24.70	-.62	14.44	-1.24	-10.10			-1.07	-13.07	-1.24	-14.97	-.71	9.29	.62	18.70
-1.07	-4.75	-.18	23.10	-.45	23.38	-1.07	-8.25			-.89	-7.97	-1.07	-13.42	-.53	28.73	.71	12.05
-.89	-3.90	0	23.20	.41	24.15	-.71	.05			-.71	9.64	-.89	-7.67	-.36	32.27	.89	-.55
-.71	-3.25	.18	25.40	.39	23.85	-.53	17.10			-.53	25.24	-.71	12.29	.53	29.20	1.07	-7.05
-.62	-1.70	.36	23.90	.46	22.85	-.36	19.65			-.44	27.04	-.53	25.84	.89	-8.10	1.24	-12.25
-.53	1.95	.53	17.40	.48	22.35					-.18	30.45	.53	19.12	1.07	-12.55	1.42	-13.60
-.44	7.40	.71	12.00	.52	21.35					0	30.87	.71	7.73	1.24	-13.70	1.78	-10.88
-.41	8.30	.89	-4.40	.53	17.35					.53	17.62	.89	-14.22	1.42	-12.75	2.13	-8.72
-.36	8.85	1.07	-11.95	.62	14.40					.62	13.98	1.07	-15.72	1.78	-9.75	2.49	-7.15
-.27	9.25	1.24	-10.00	.71	6.15					.89	-10.92	1.24	-14.01	2.13	-7.75	3.20	-4.85
-.18	9.15	1.42	-9.00	.89	-7.15					1.07	-15.27	1.42	-12.26	2.49	-6.15	3.56	-4.20
0	8.05	1.78	-6.45	1.07	-10.45					1.24	-14.56	1.78	-8.25	2.84	-5.08	3.91	-3.59
.18	8.45	2.13	-4.80	1.24	-9.55					1.42	-12.76	2.13	-6.33	3.56	-3.60	4.27	-3.07
.41	9.00	2.49	-3.93	1.42	-8.65					1.78	-8.70	2.49	-4.96	4.27	-2.53	4.62	-2.70
.53	7.15	3.20	-2.56	1.78	-6.35					2.13	-6.58	2.84	-3.85			4.98	-2.35
.71	-.50	3.56	-2.25	2.49	-3.53					2.49	-5.06	3.56	-3.95			5.33	-2.00
.89	-3.80	3.91	-1.90	3.20	-2.51					2.84	-3.70	4.27	-2.85				
1.07	-4.35	4.27	-1.60	3.91	-2.00					3.20	-3.60	4.98	-1.86				
1.24	-4.25	4.62	-1.45	4.63	-1.55					3.56	-3.95	5.67	-1.27				
1.42	-3.55	4.98	-1.20	5.34	-1.10					4.27	-2.85						
1.78	-2.55	5.33	-1.07							4.98	-1.91						
										5.67	-1.27						

TABLE II.- EXPERIMENTAL DOWNWASH ANGLES MEASURED THROUGH MODEL VORTICES AT MACH NUMBER 1.98, Re = 0.13×10^6 PER INCH

(a) $\alpha = 15^\circ$; x/d = 8.8; z/a = 1.61		(b) $\alpha = 15^\circ$; x/d = 10.2; z/a = 1.82	
y/a	ϵ, deg	y/a	ϵ, deg
-6.75	-0.95	-6.40	-0.80
-6.40	-1.05	-5.70	-.80
-5.67	-1.25	-4.98	-1.30
-4.98	-1.50	-4.27	-1.70
-4.27	-1.75	-3.56	-2.40
-3.56	-2.45	-2.85	-3.38
-2.84	-3.20	-2.49	-4.20
-2.49	-4.02	-2.13	-5.38
-2.13	-5.19	-1.78	-7.10
-1.78	-6.90	-1.42	-9.73
-1.42	-10.06	-1.24	-9.90
-1.24	-10.83	-1.07	-9.96
-1.07	-10.84	-.89	-9.12
-.89	-10.15	-.80	-4.52
-.71	6.83	-.71	6.77
-.71	6.88	-.62	16.07
-.57	21.90	.38	24.33
-.36	19.91	.44	22.33
-.18	24.88	.53	16.82
0	24.92	.62	13.92
.18	25.29	.71	5.31
.36	19.93	.89	-9.00
.36	20.48	1.07	-9.23
.53	17.62	1.24	-9.10
.71	6.31	1.42	-8.83
.89	-7.60	1.78	-6.60
1.07	-9.81	2.49	-3.86
1.24	-10.08	3.20	-2.57
1.42	-9.44	3.91	-1.88
1.78	-6.65	4.63	-1.44
2.13	-5.05	5.34	-1.05
2.49	-3.80		
2.84	-3.25		
3.56	-2.35		
4.27	-1.65		
4.98	-1.30		
5.33	-1.30		
5.67	-1.30		

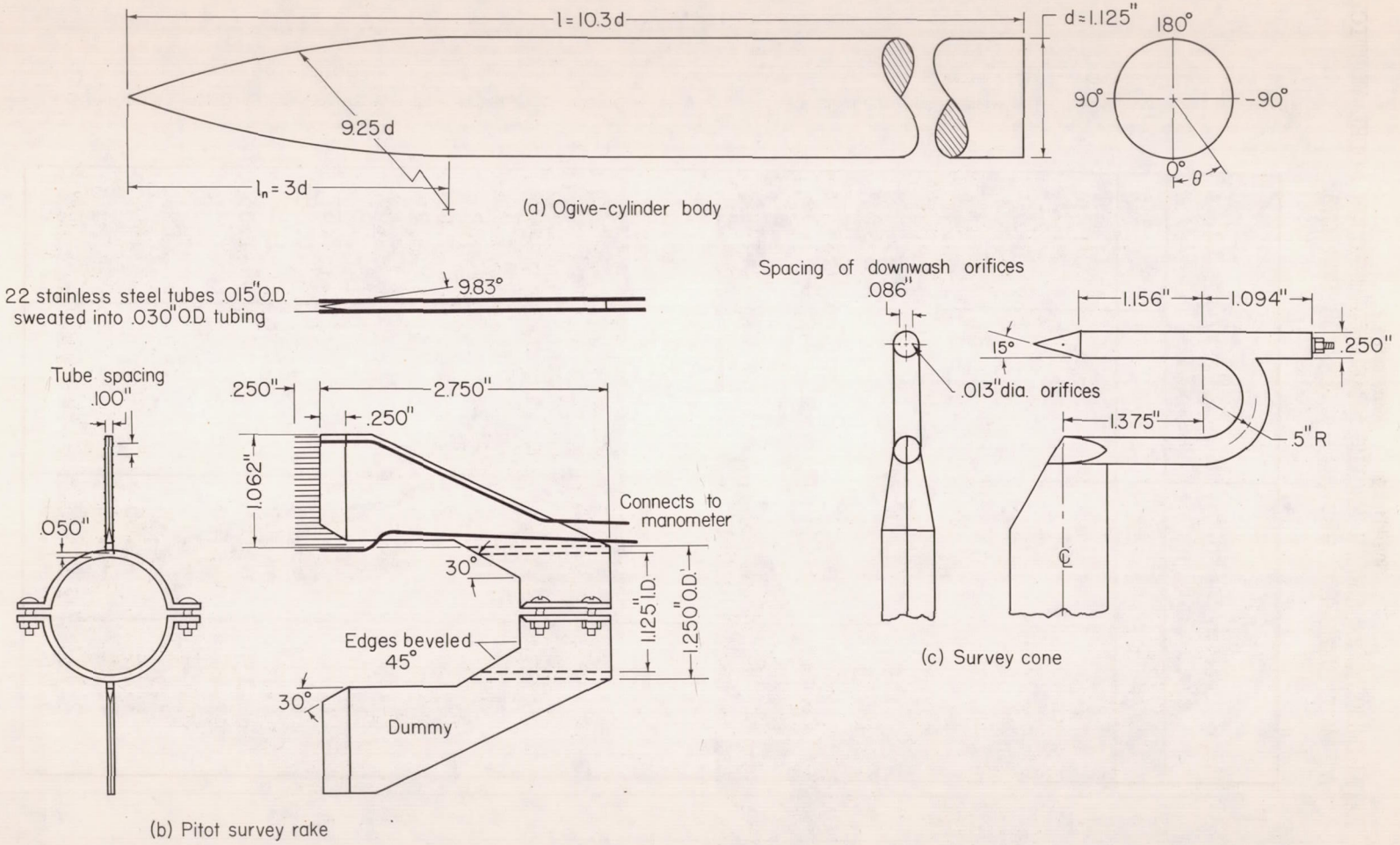
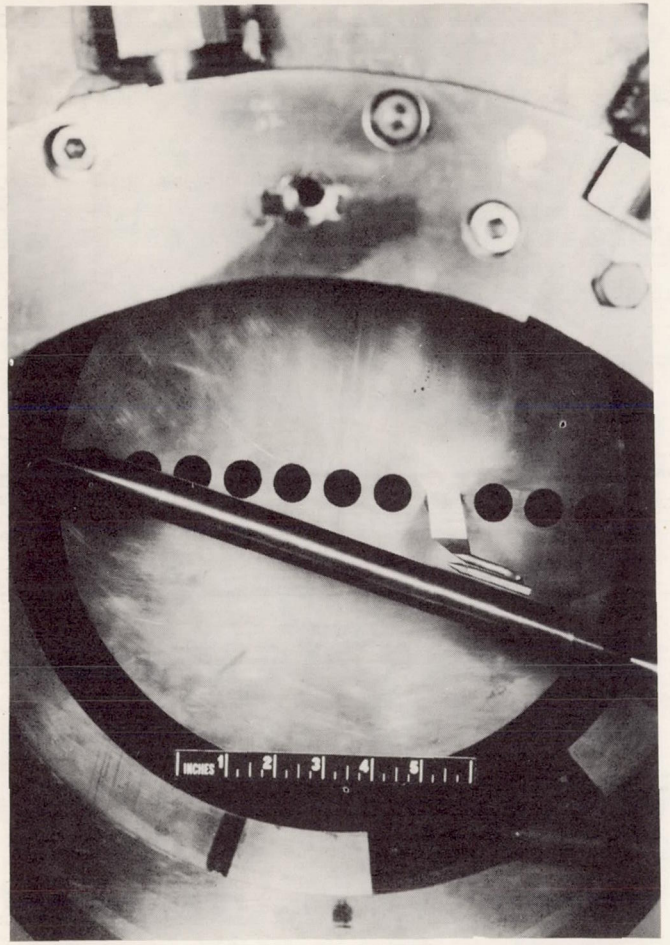
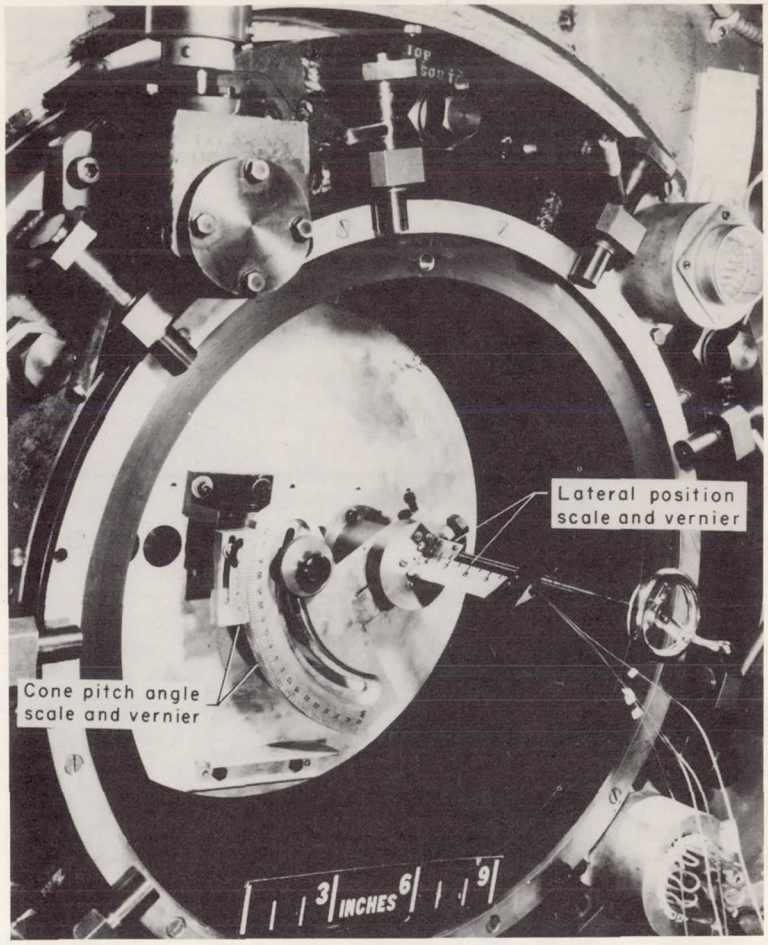


Figure 1.- Model and survey apparatus.



A-18408

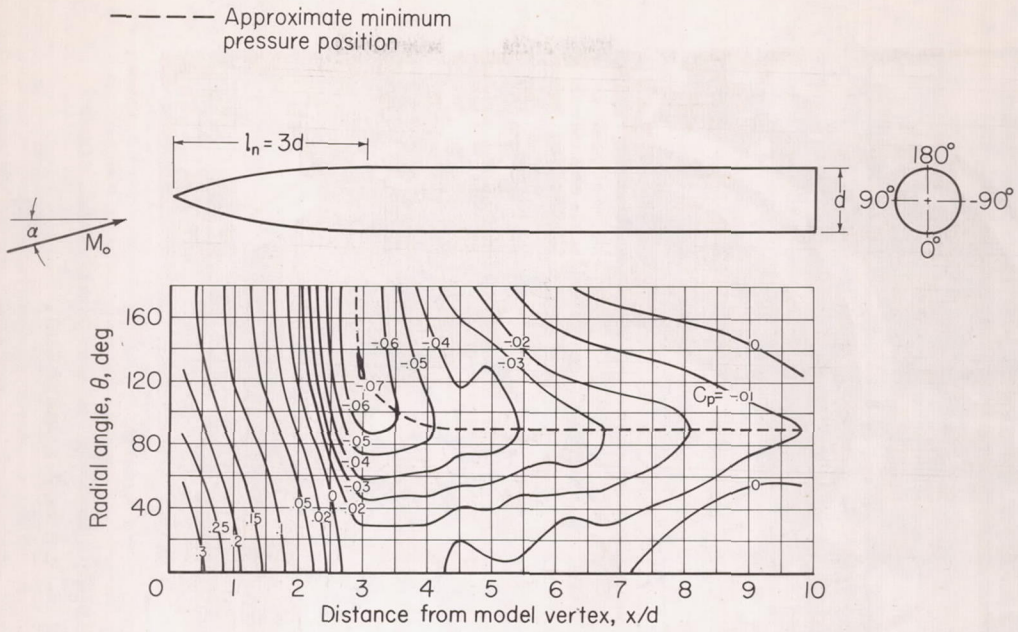
(d) Model and survey cone mounted in wind tunnel.



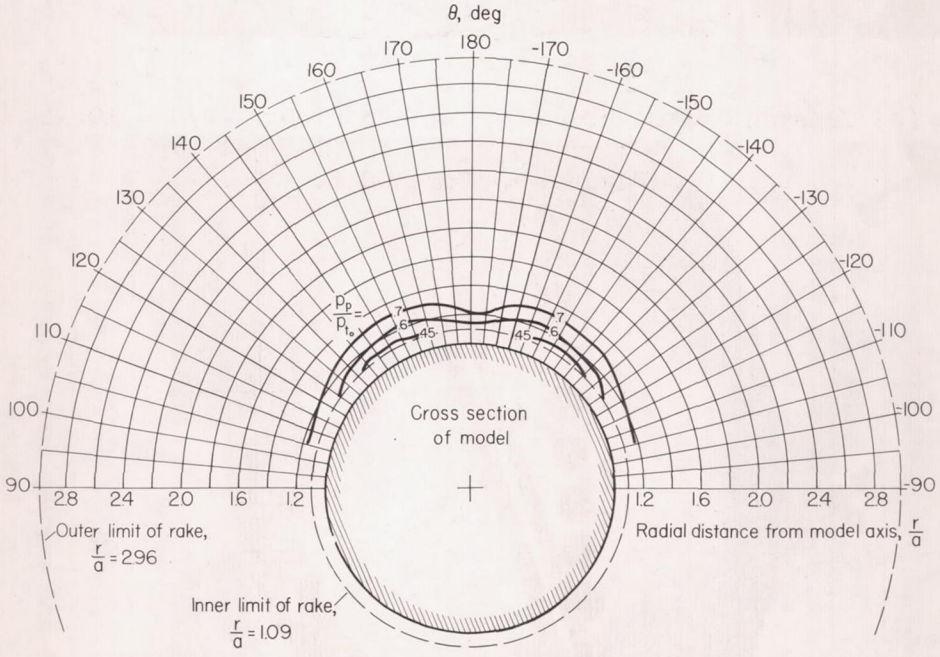
A-18409.1

(e) Exterior view of side plate and cone survey apparatus.

Figure 1.- Concluded.

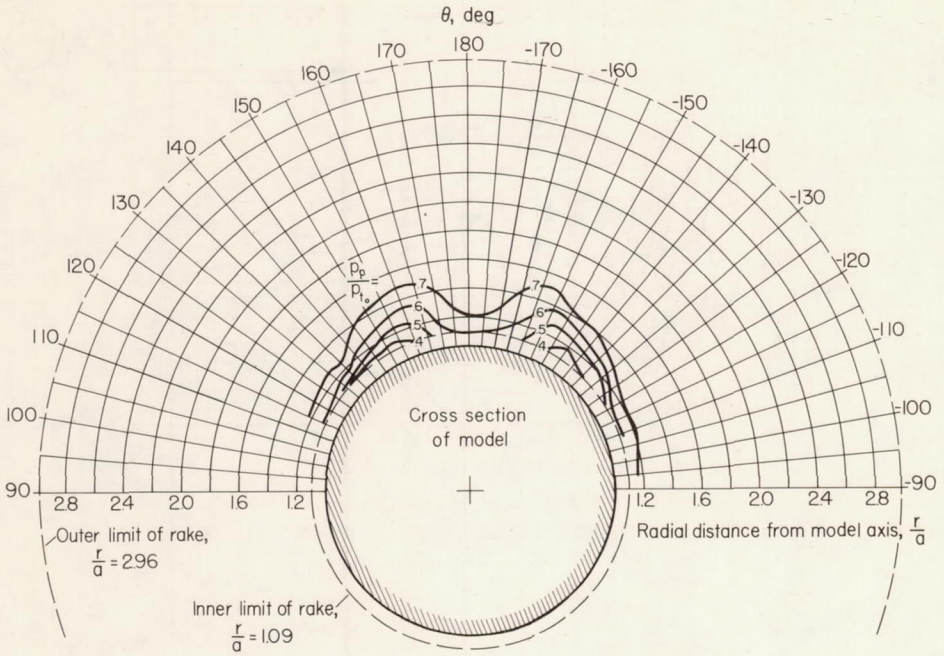


(a) Constant pressure-coefficient contours.



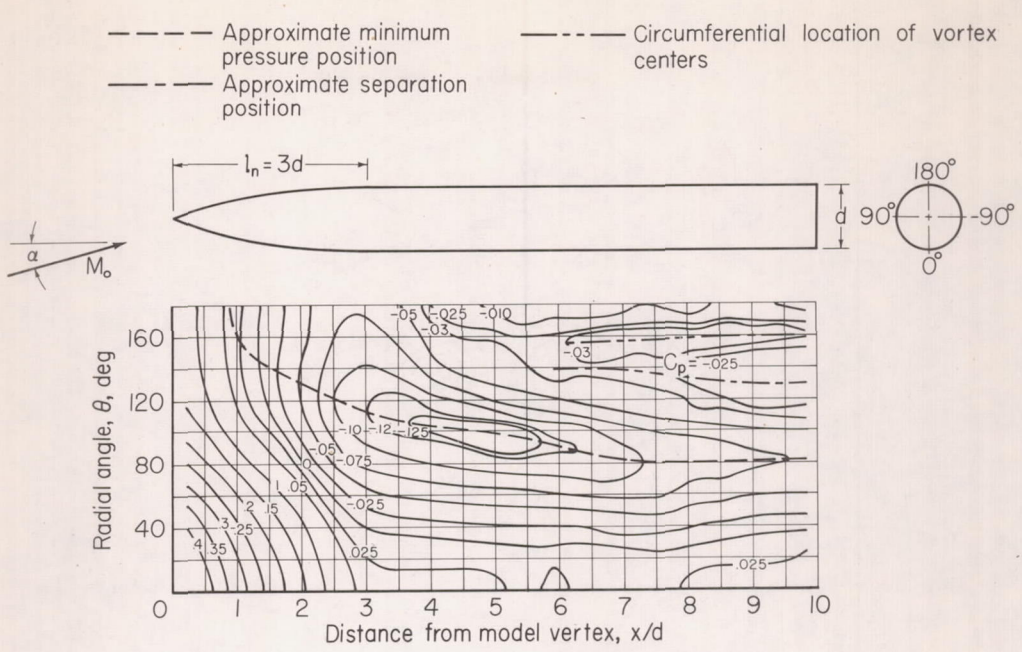
(b) Constant pitot-pressure ratio contours, x/d = 7.61.

Figure 2.- Experimental contours of pressure coefficient on the body and pitot to free-stream total-pressure ratio in the flow field, M_o = 1.98; Re = 0.39×10^6 per inch; $\alpha = 5^o$.

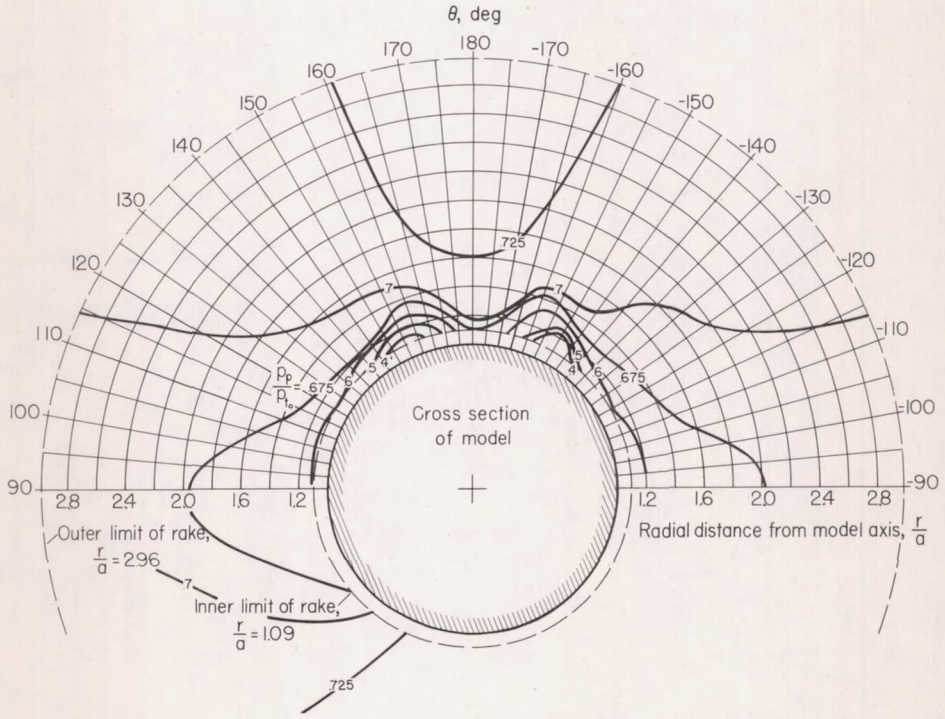


(c) Constant pitot-pressure ratio contours, x/d = 10.28.

Figure 2.- Concluded.

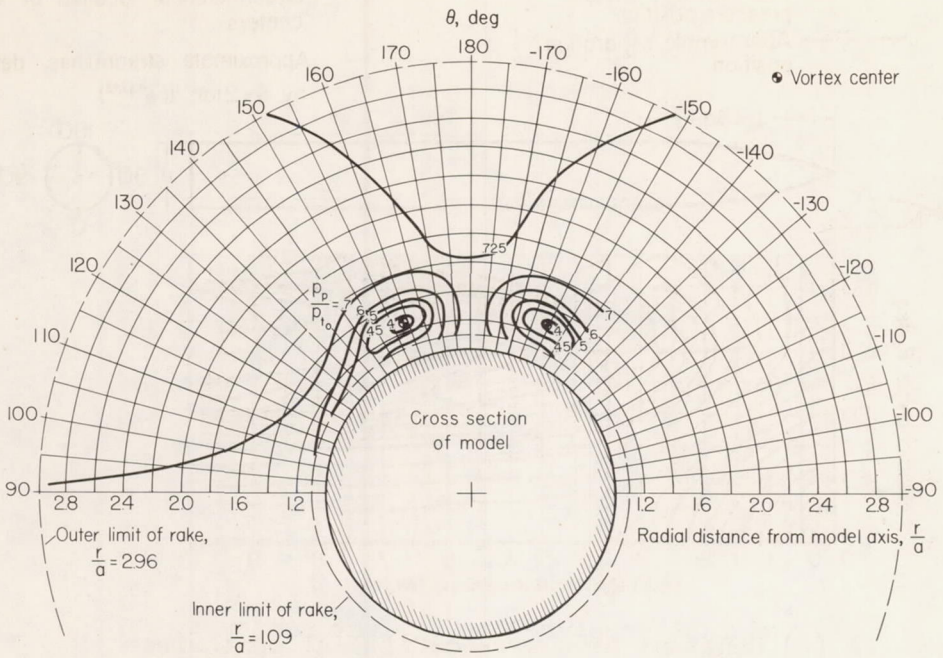


(a) Constant pressure-coefficient contours.

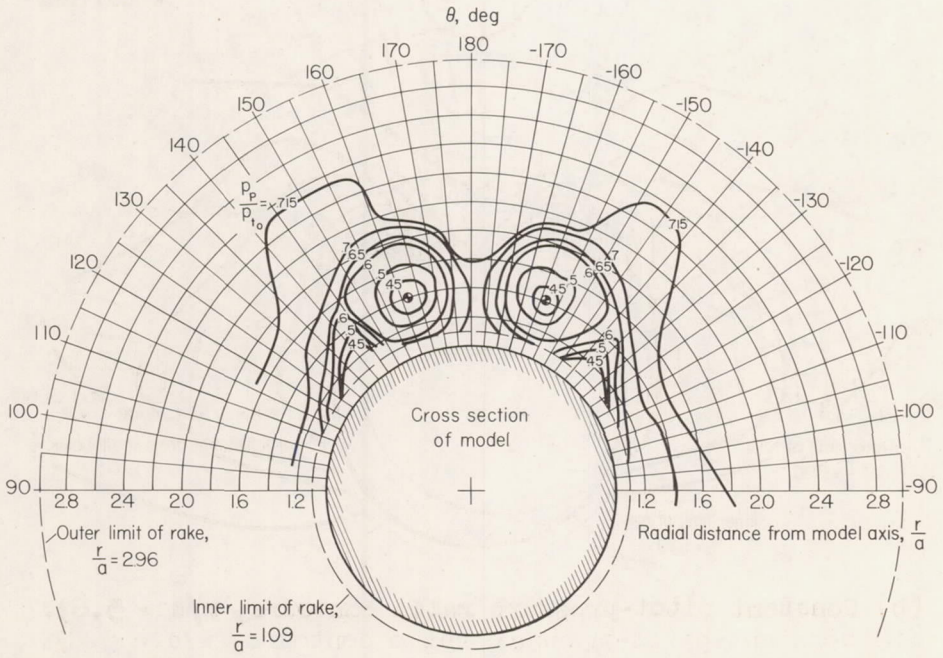


(b) Constant pitot-pressure ratio contours, x/d = 5.83.

Figure 3.- Experimental contours of pressure coefficient on the body and pitot to free-stream total-pressure ratio in the flow field, $M_o = 1.98$; Re = 0.39×10^6 per inch; $\alpha = 10^o$.

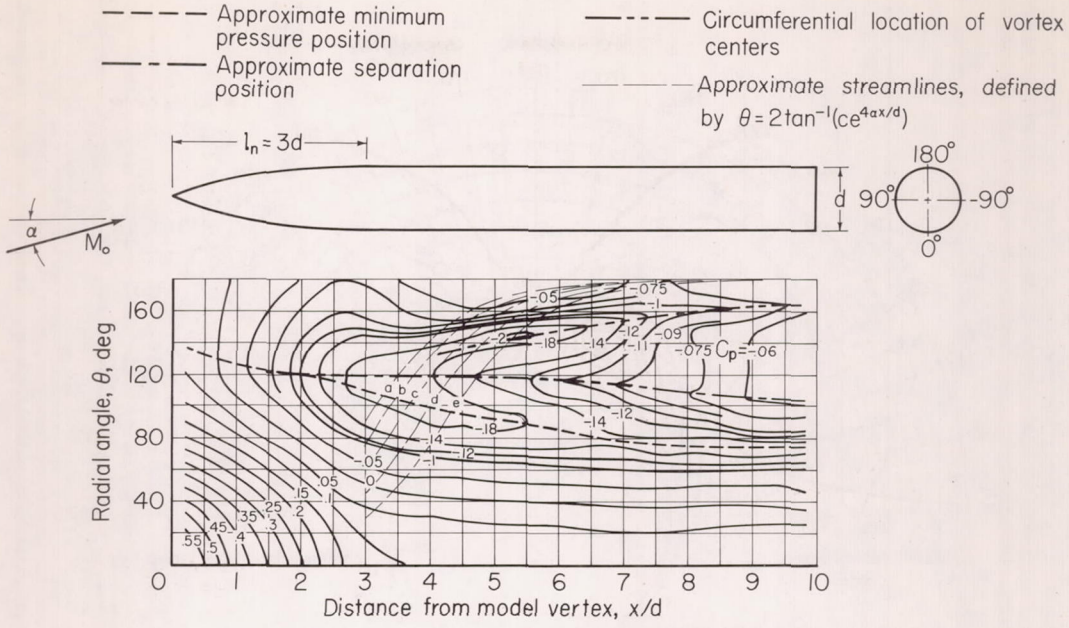


(c) Constant pitot-pressure ratio contours, x/d = 7.61.

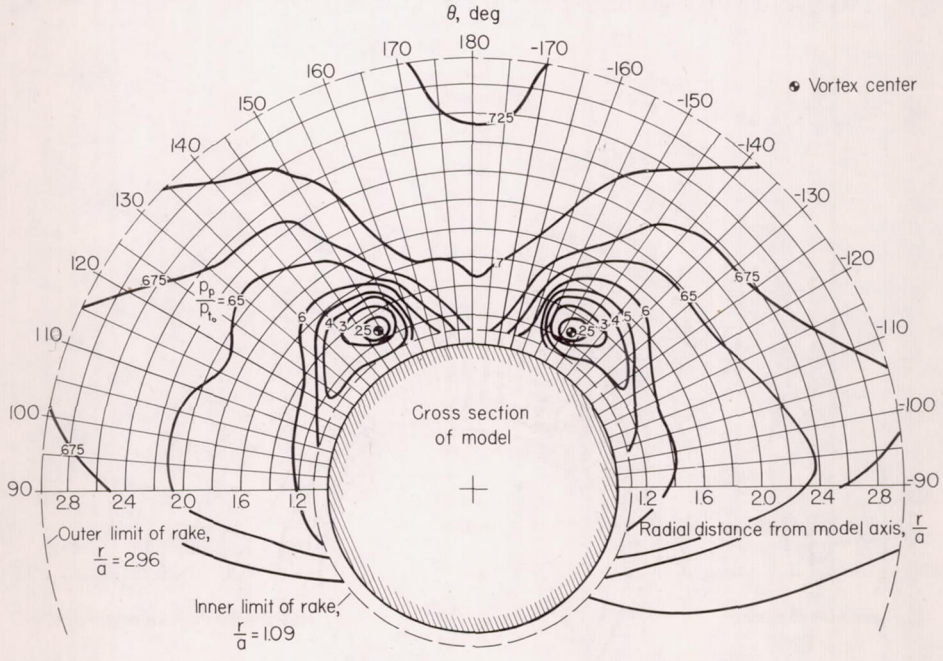


(d) Constant pitot-pressure ratio contours, x/d = 10.28.

Figure 3.- Concluded.

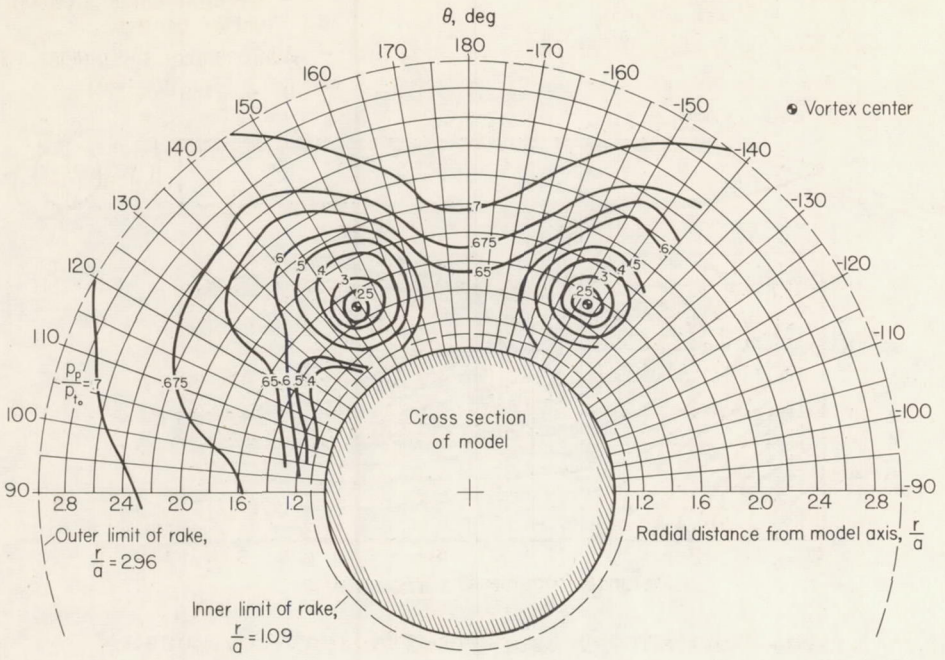


(a) Constant pressure-coefficient contours.

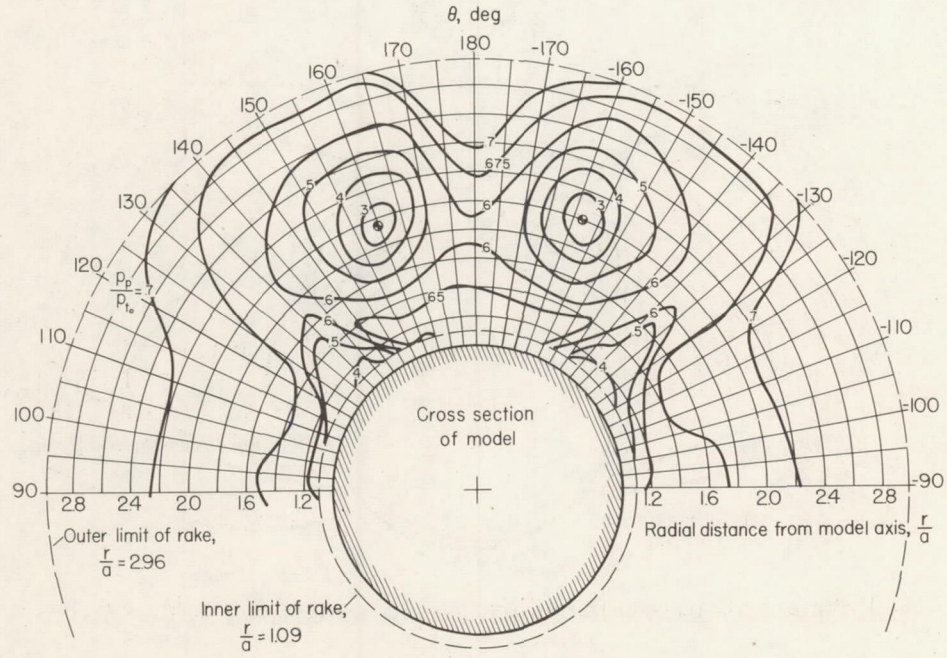


(b) Constant pitot-pressure ratio contours, x/d = 5.83.

Figure 4.- Experimental contours of pressure coefficient on the body and pitot to free-stream total-pressure ratio in the flow field, M_o = 1.98; Re = 0.39×10^6 per inch; α = 15°.

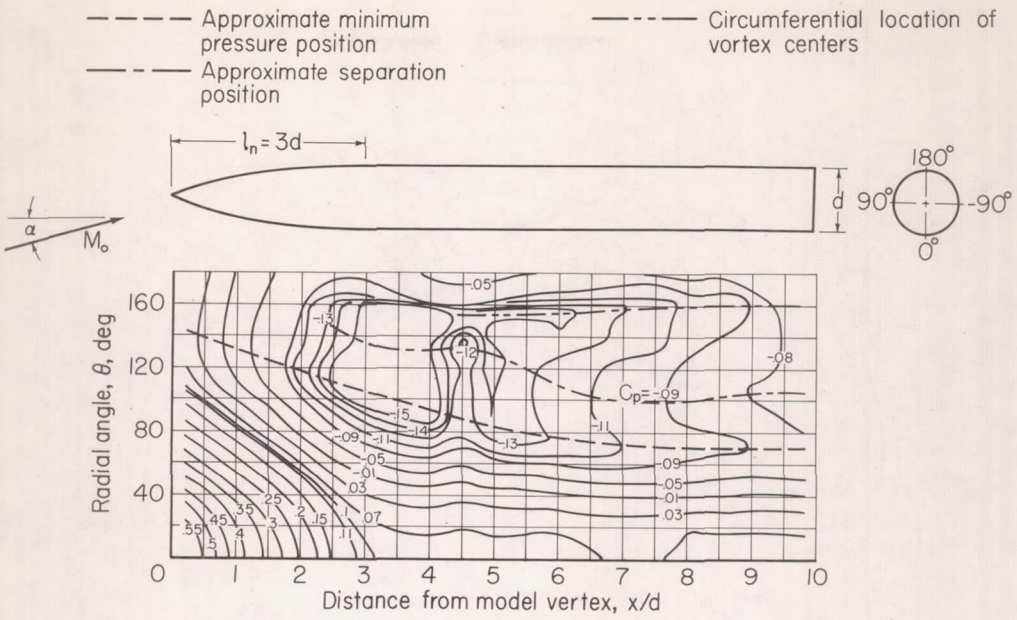


(c) Constant pitot-pressure ratio contours, x/d = 7.61.

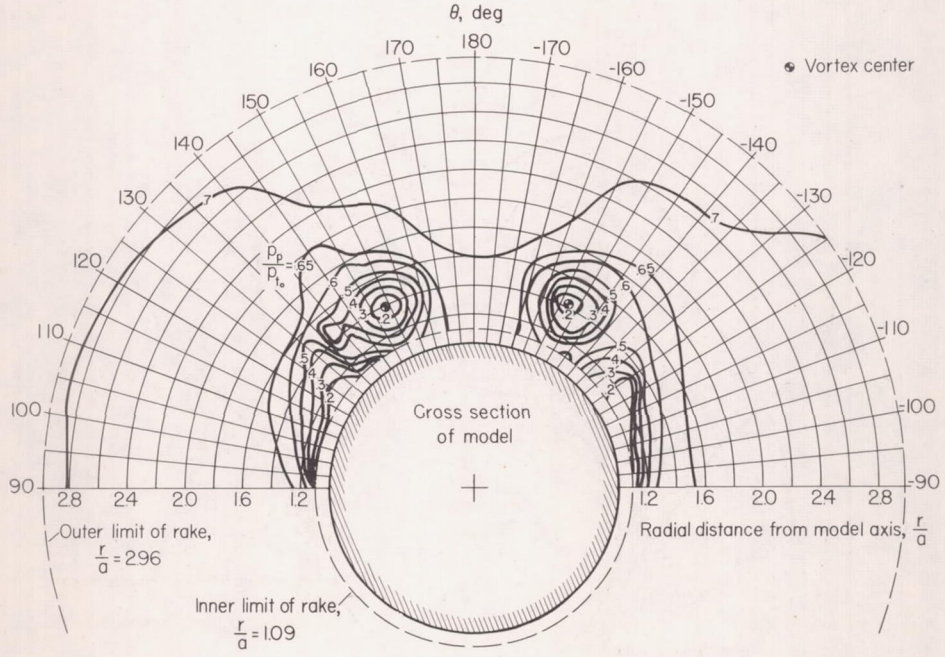


(d) Constant pitot-pressure ratio contours, x/d = 10.28.

Figure 4.- Concluded.

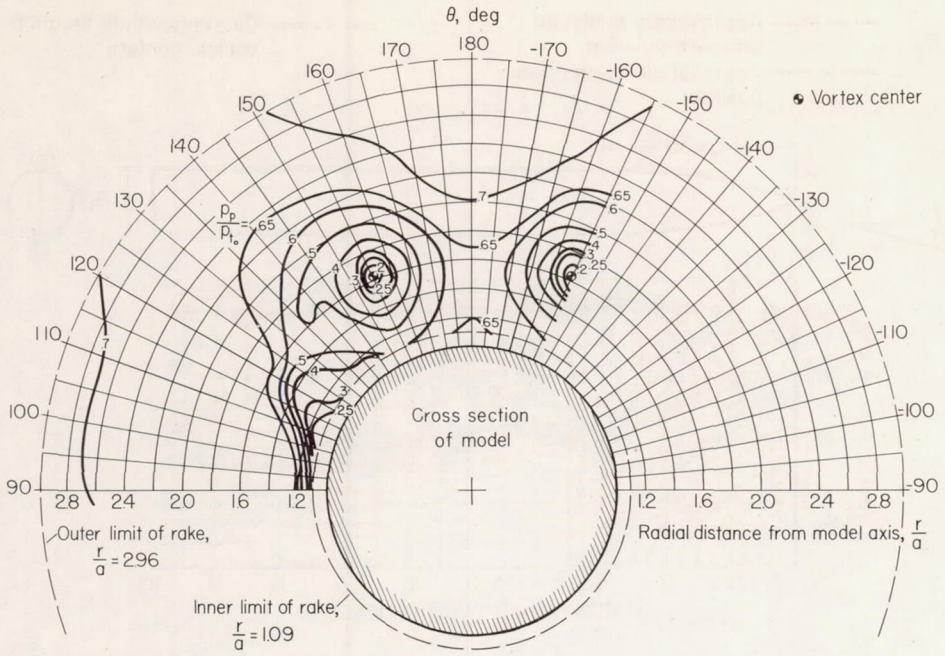


(a) Constant pressure-coefficient contours.

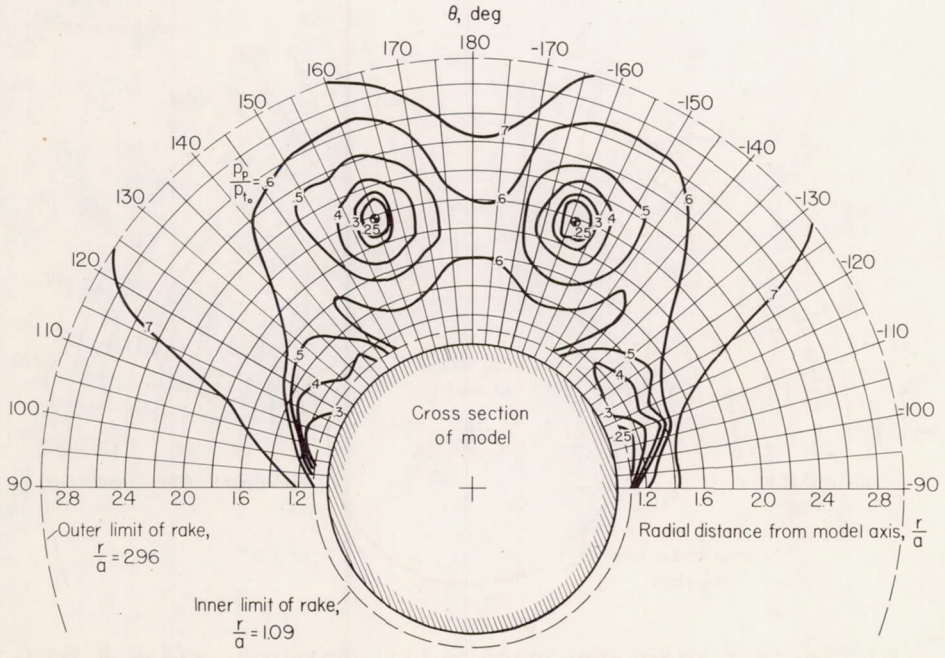


(b) Constant pitot-pressure ratio contours, x/d = 5.83.

Figure 5.- Experimental contours of pressure coefficient on the body and pitot to free-stream total-pressure ratio in the flow field, M_o = 1.98; Re = 0.13×10^6 per inch; α = 15°.

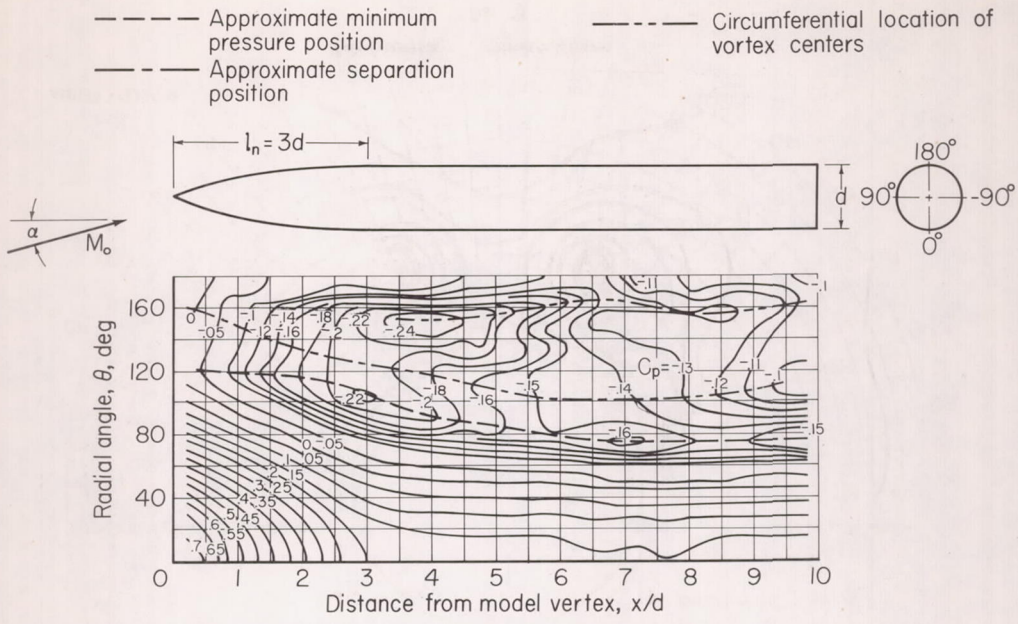


(c) Constant pitot-pressure ratio contours, x/d = 7.61.

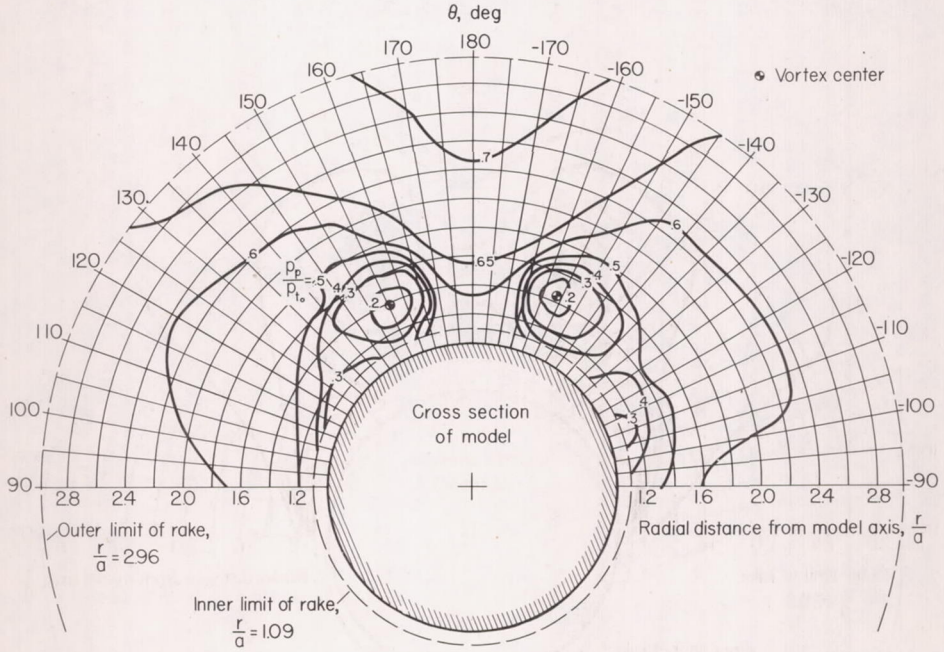


(d) Constant pitot-pressure ratio contours, x/d = 10.28.

Figure 5.- Concluded.

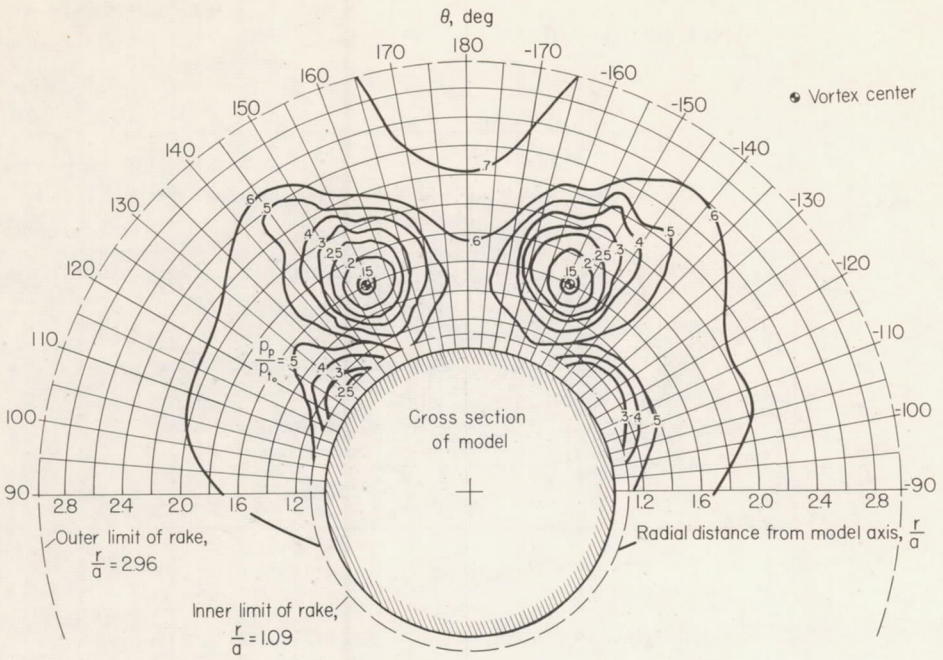


(a) Constant pressure-coefficient contours.

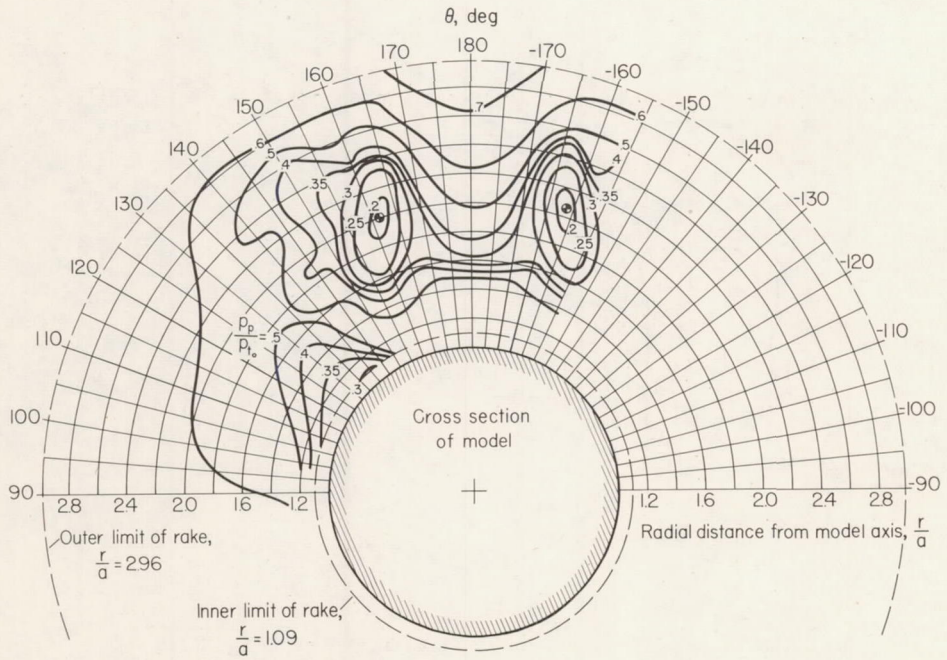


(b) Constant pitot-pressure ratio contours, x/d = 4.50.

Figure 6.- Experimental contours of pressure coefficient on the body and pitot to free-stream total-pressure ratio in the flow field, M_o = 1.98; Re = 0.39×10^6 per inch; α = 20°.

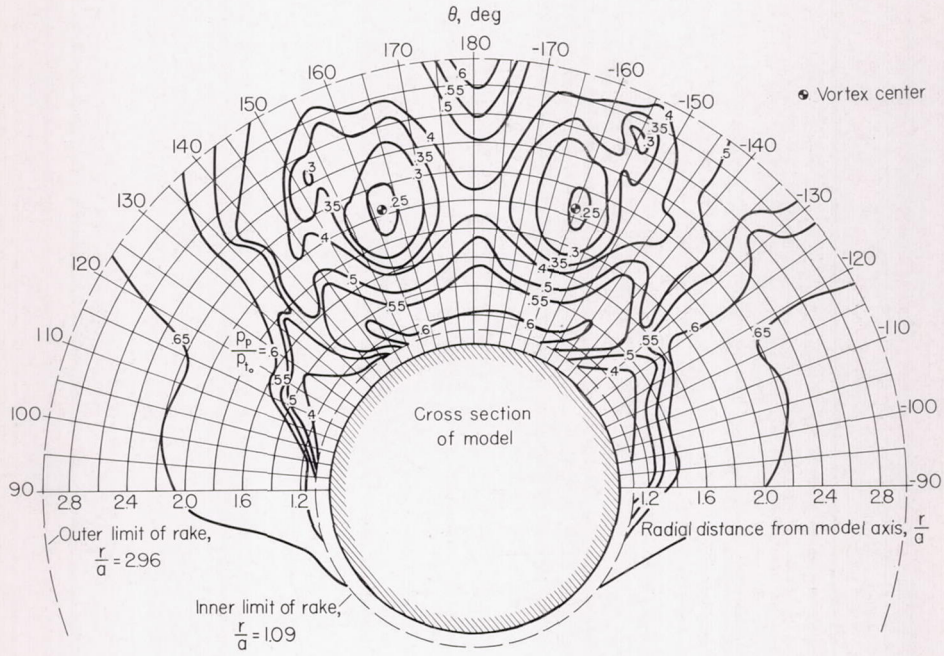


(c) Constant pitot-pressure ratio contours, x/d = 5.83.



(d) Constant pitot-pressure ratio contours, x/d = 7.61.

Figure 6.- Continued.



(e) Constant pitot-pressure ratio contours, x/d = 10.28.

Figure 6.- Concluded.

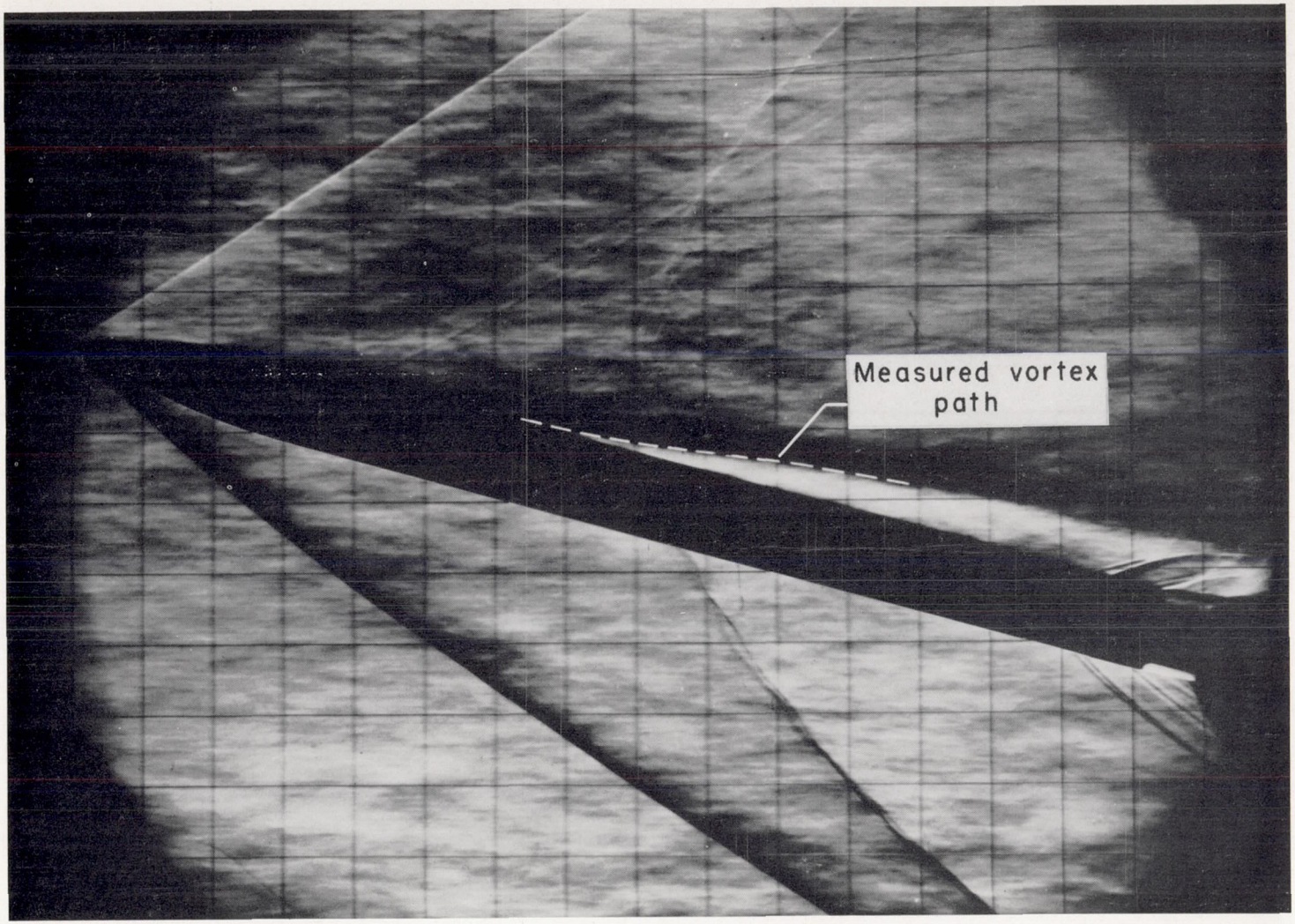
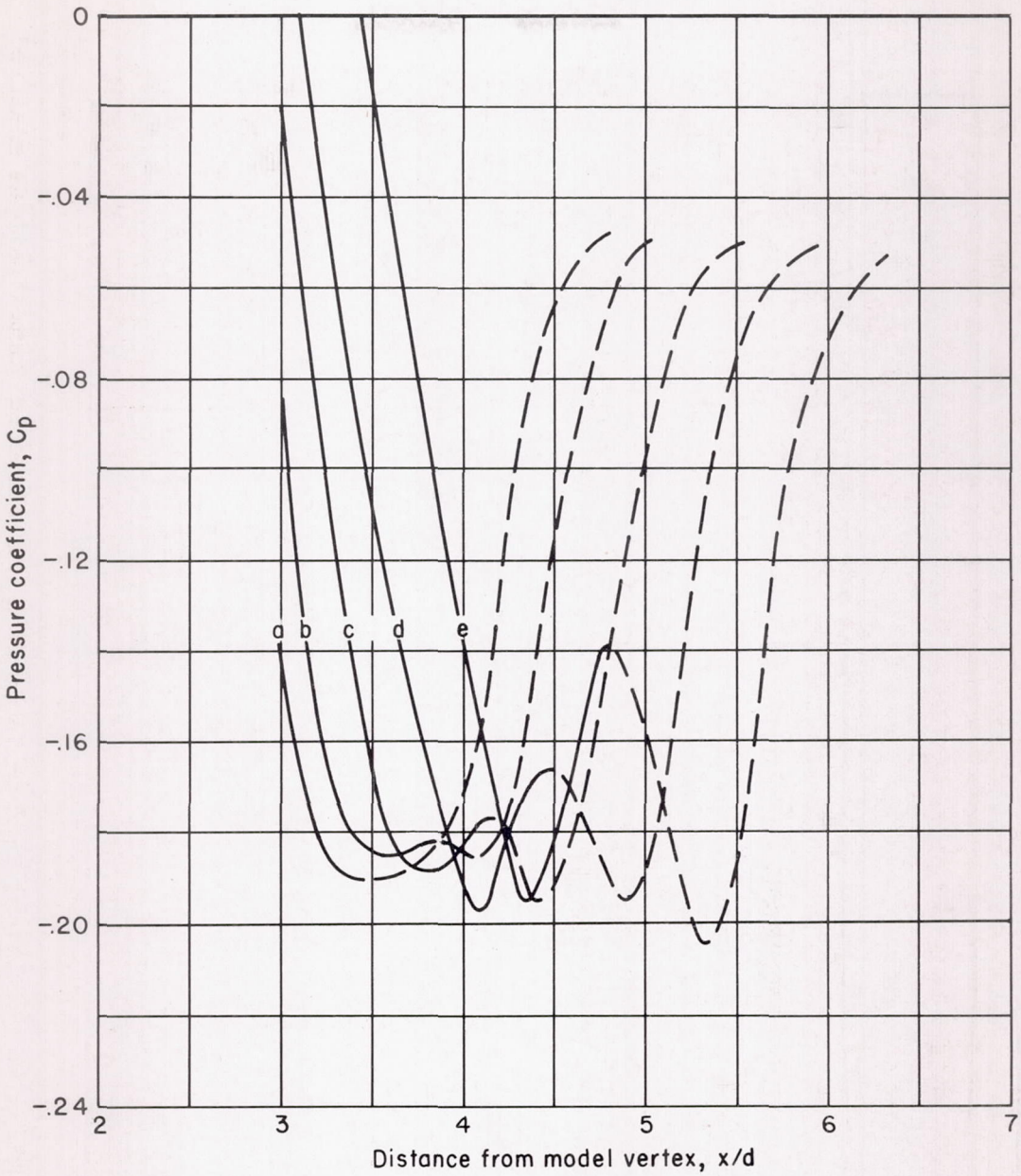


Figure 7.- Typical schlieren photograph of flow field with superimposed vortex path as measured from pitot-rake surveys, α = 15; Re = 0.39×10^6 per inch; M_o = 1.98.



(a) $\alpha = 10^{\circ}$, $x/d = 10.3$

Figure 8.- Pressure distributions along the streamlines shown in figure 4, $M_o = 1.98$; $Re = 0.39 \times 10^6$ per inch; $\alpha = 15^{\circ}$.

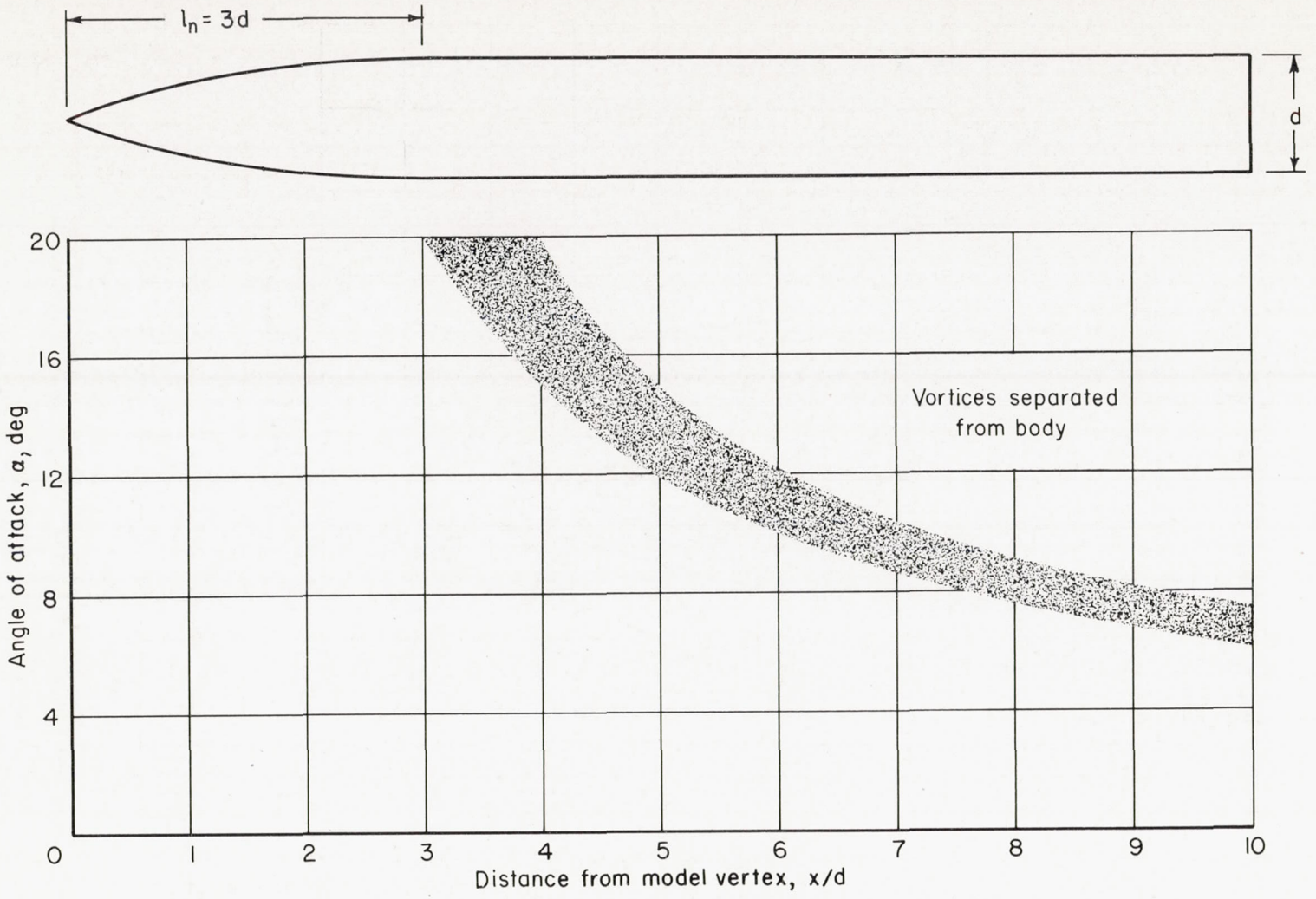


Figure 9.- Approximate body length positions at which vortices separated from body, $M_o = 1.98$.

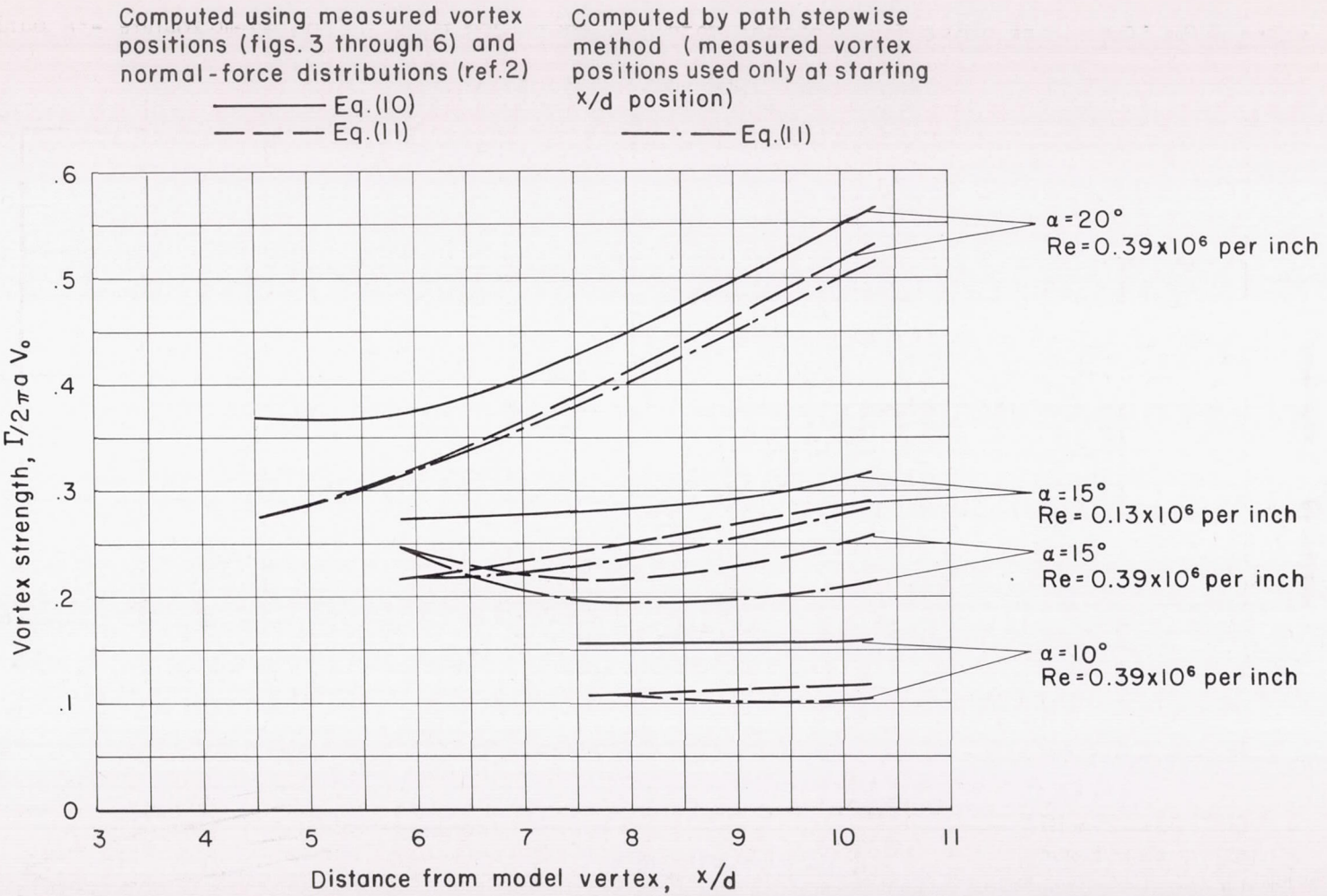
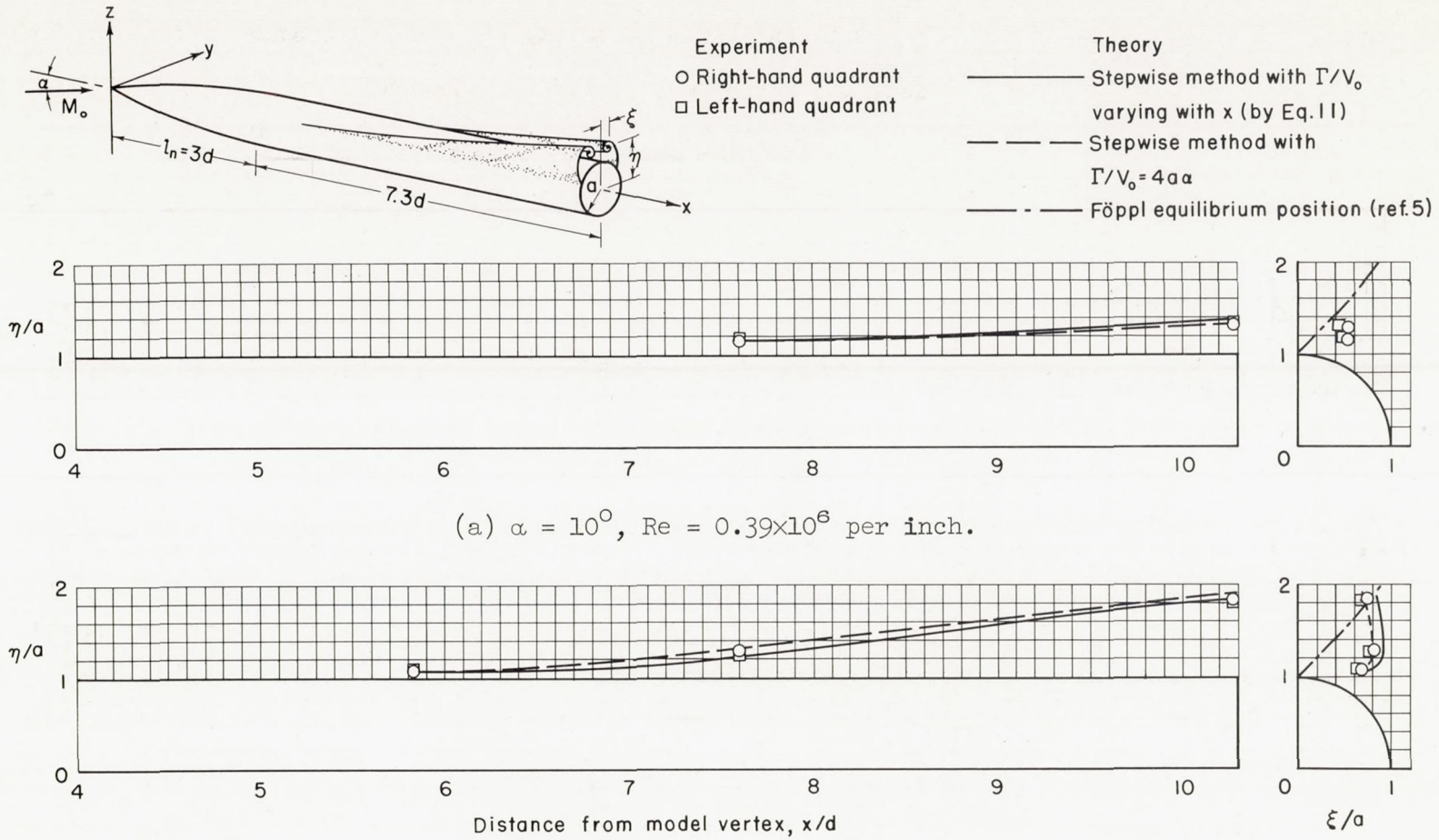


Figure 10.- Vortex strengths computed from measured vortex positions and normal-force distributions, $M_o = 1.98$.

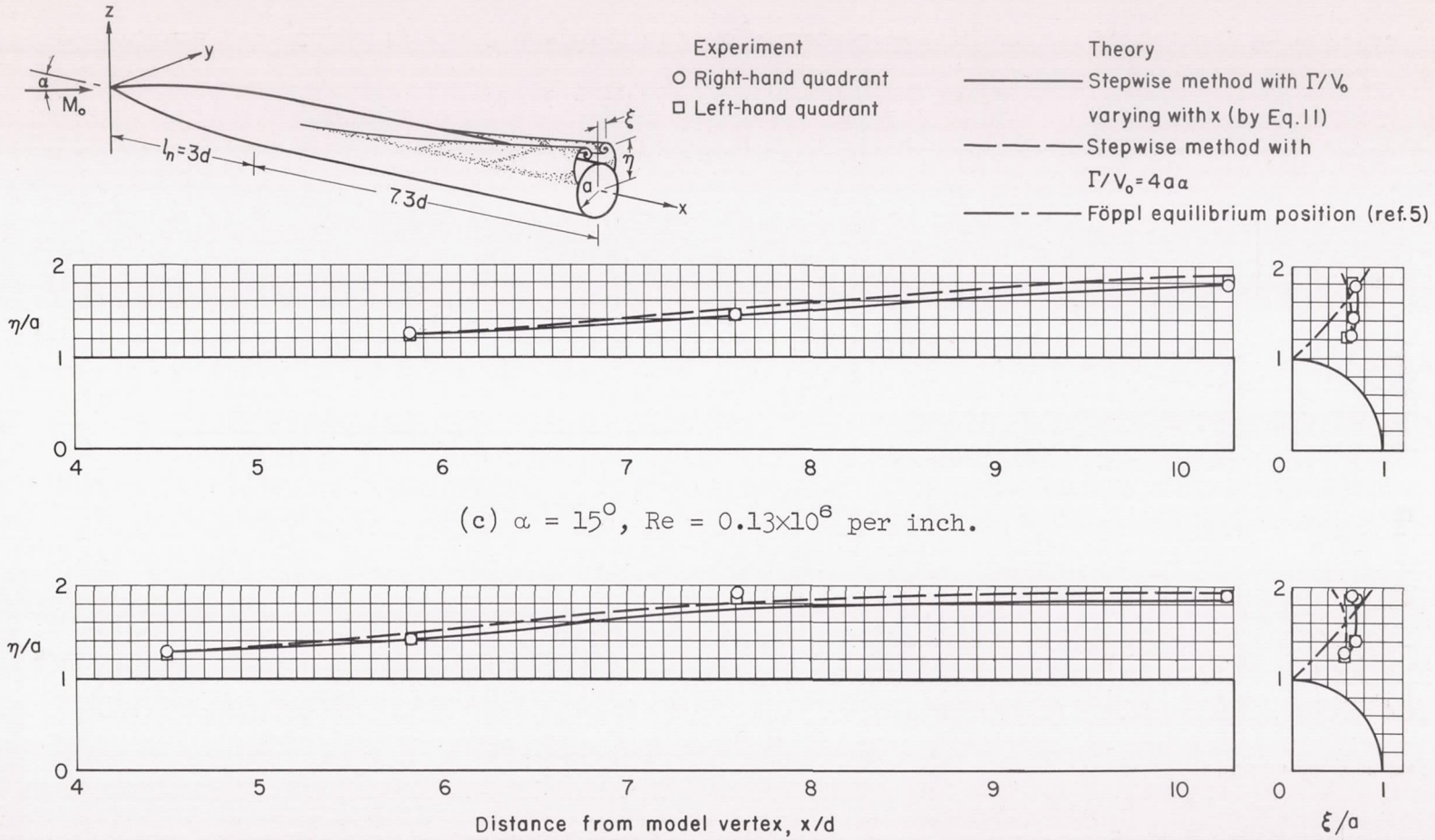


(a) $\alpha = 10^{\circ}$, Re = 0.39×10^{6} per inch.

(b) $\alpha = 15^{\circ}$, Re = 0.39×10^{6} per inch.

Figure 11.- Comparisons of computed and experimental vortex center positions, $M_0 = 1.98$.

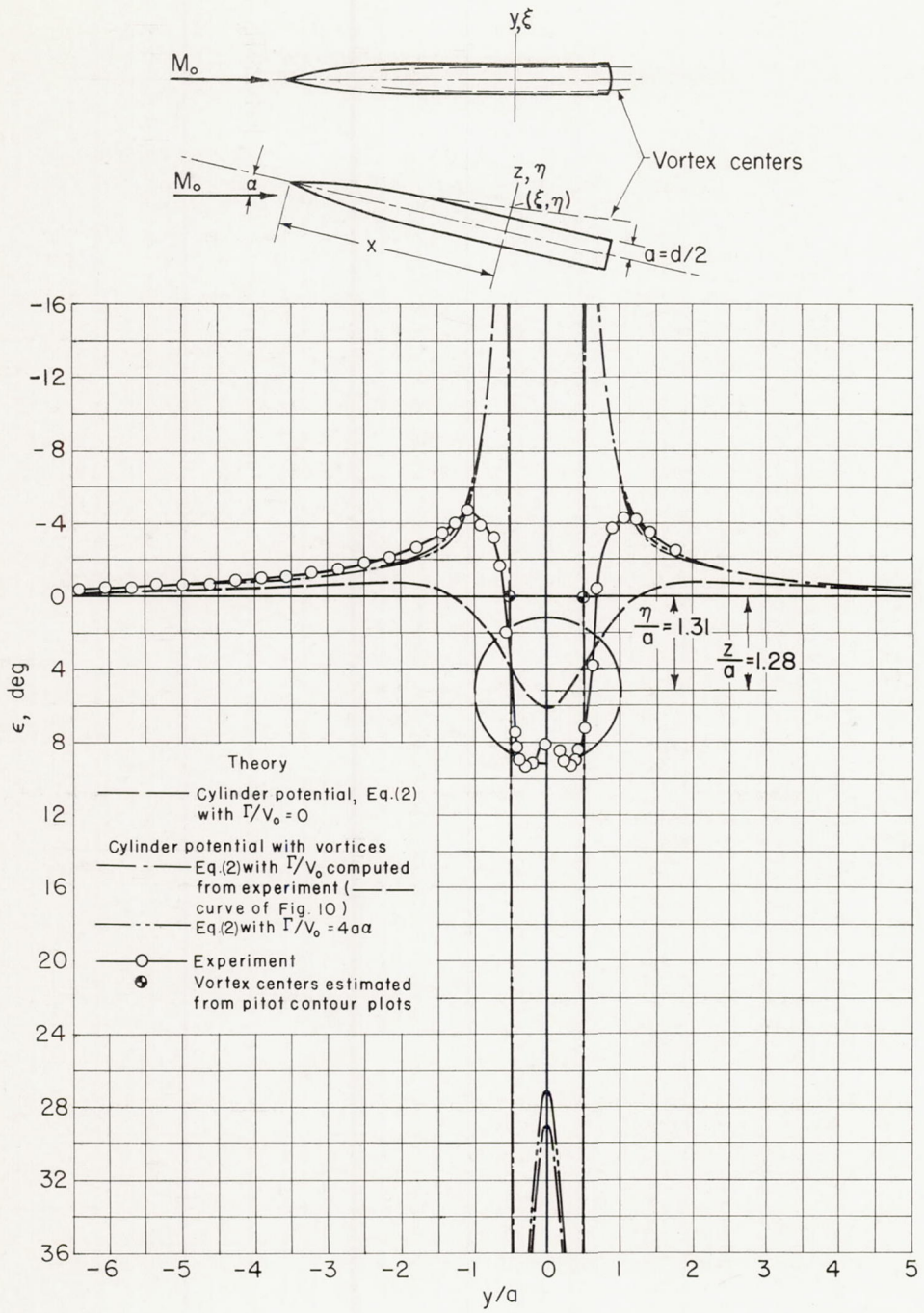
CONFIDENTIAL



(c) $\alpha = 15^{\circ}$, Re = 0.13×10^{6} per inch.

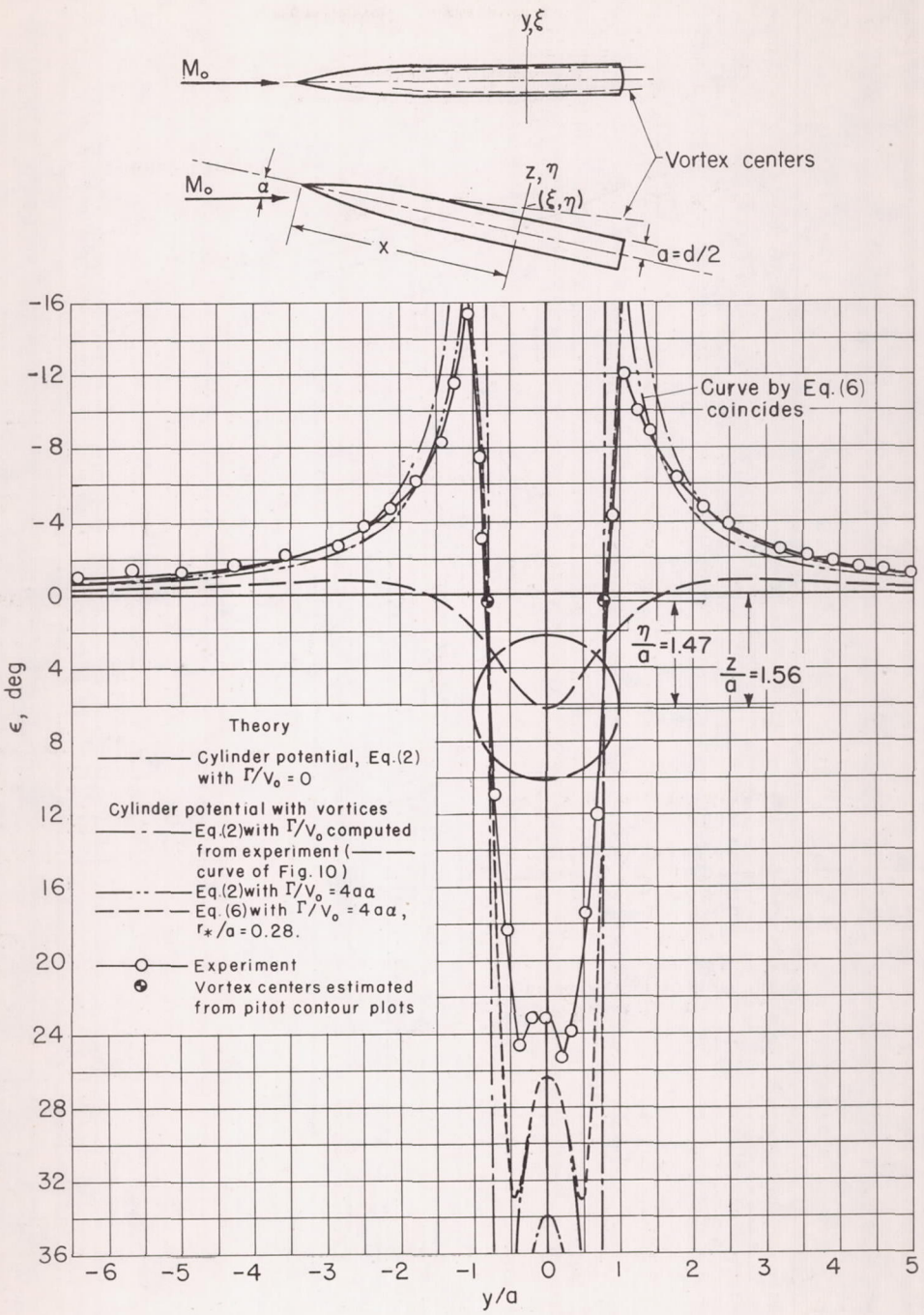
(d) $\alpha = 20^{\circ}$, Re = 0.39×10^{6} per inch.

Figure 11.- Concluded.



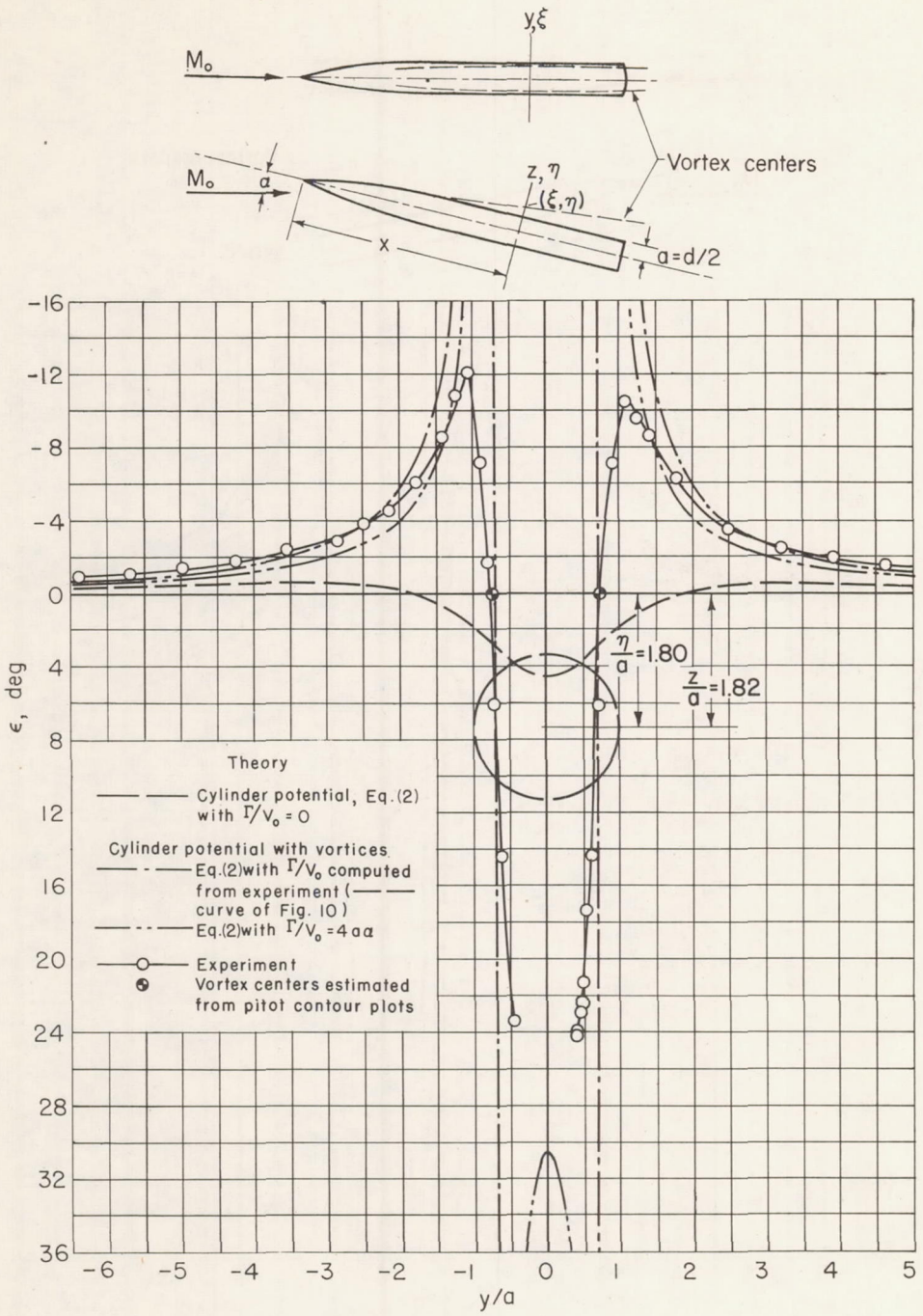
(a) $\alpha = 10^{\circ}$, x/d = 10.3

Figure 12.- Comparison of theoretical and experimental downwash distributions through body vortices for various α's and x/d stations, $M_0 = 1.98$; Re = 0.39×10^6 per inch.



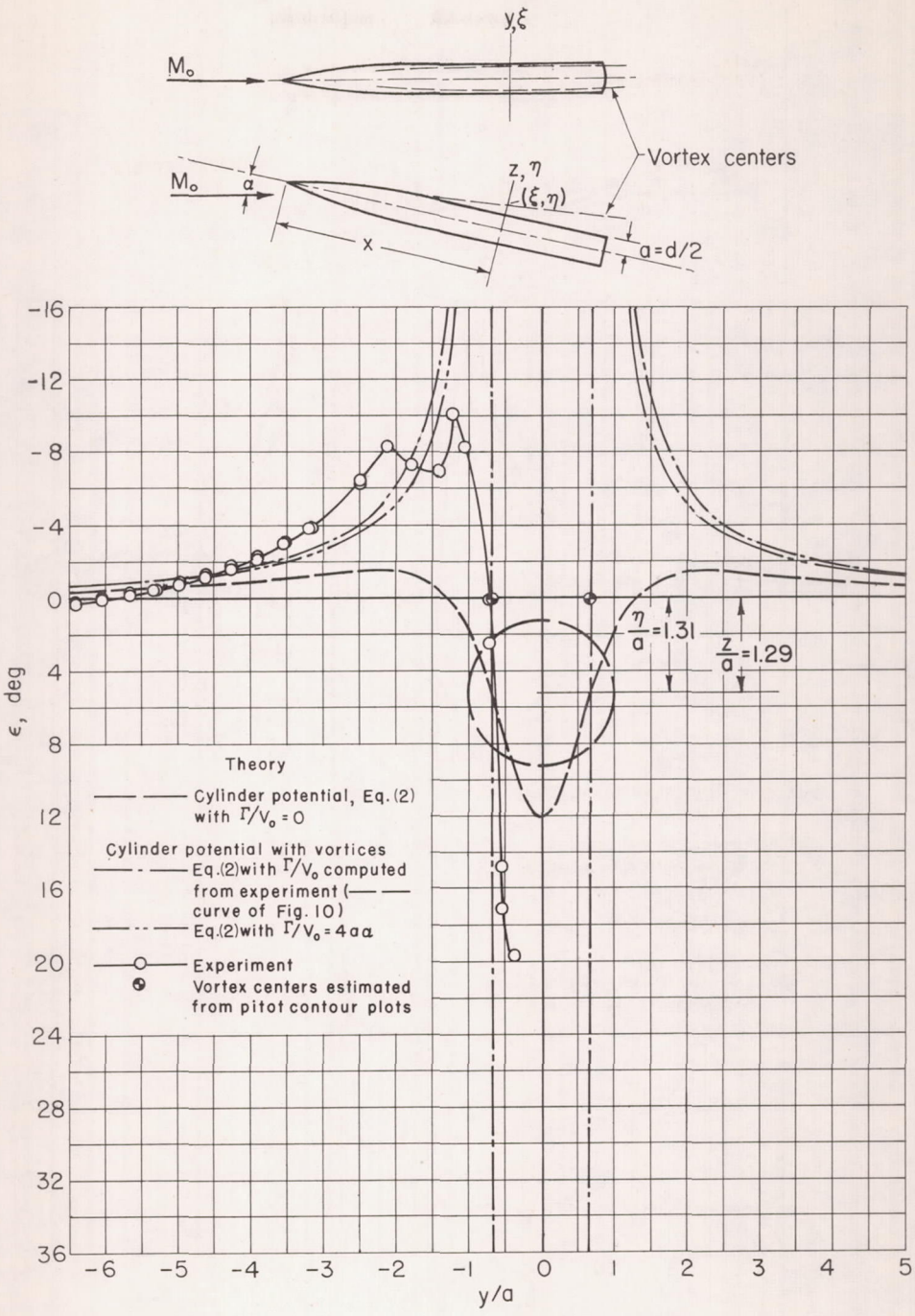
(b) $\alpha = 15^{\circ}$, $x/d = 8.8$

Figure 12.- Continued.



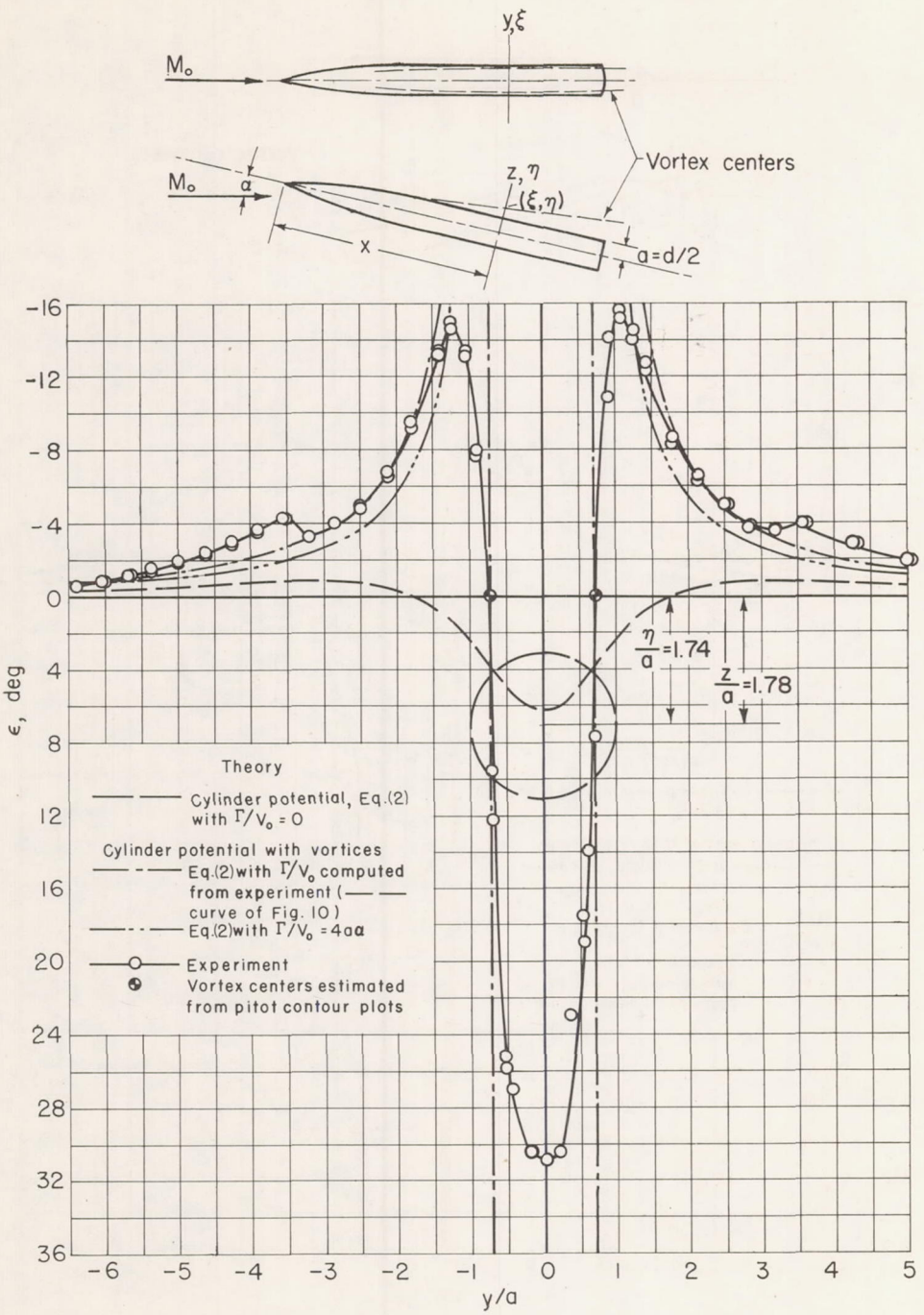
(c) $\alpha = 15^{\circ}$, $x/d = 10.2$

Figure 12.- Continued.



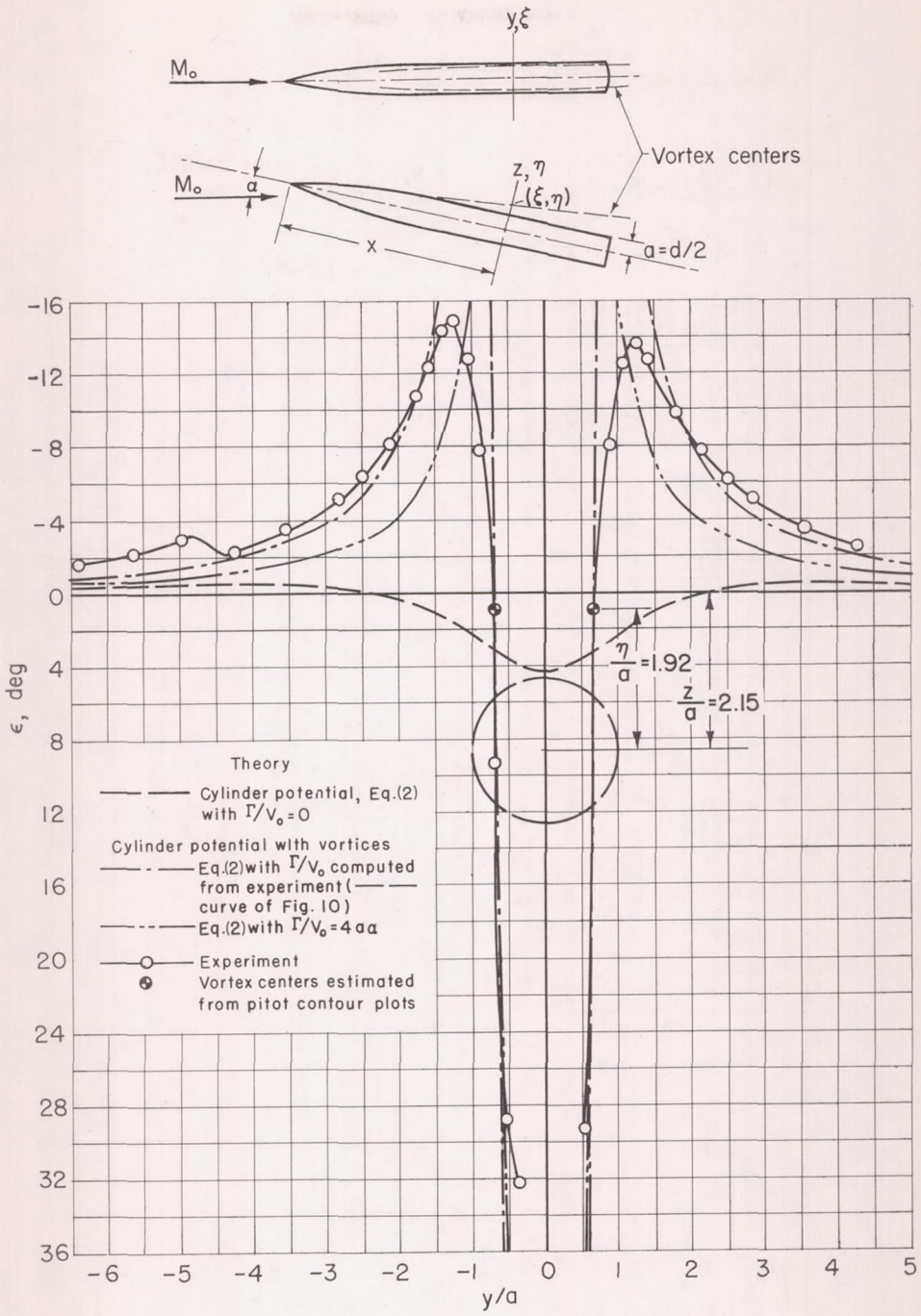
(d) $\alpha = 20^{\circ}$, $x/d = 5.1$

Figure 12.- Continued.



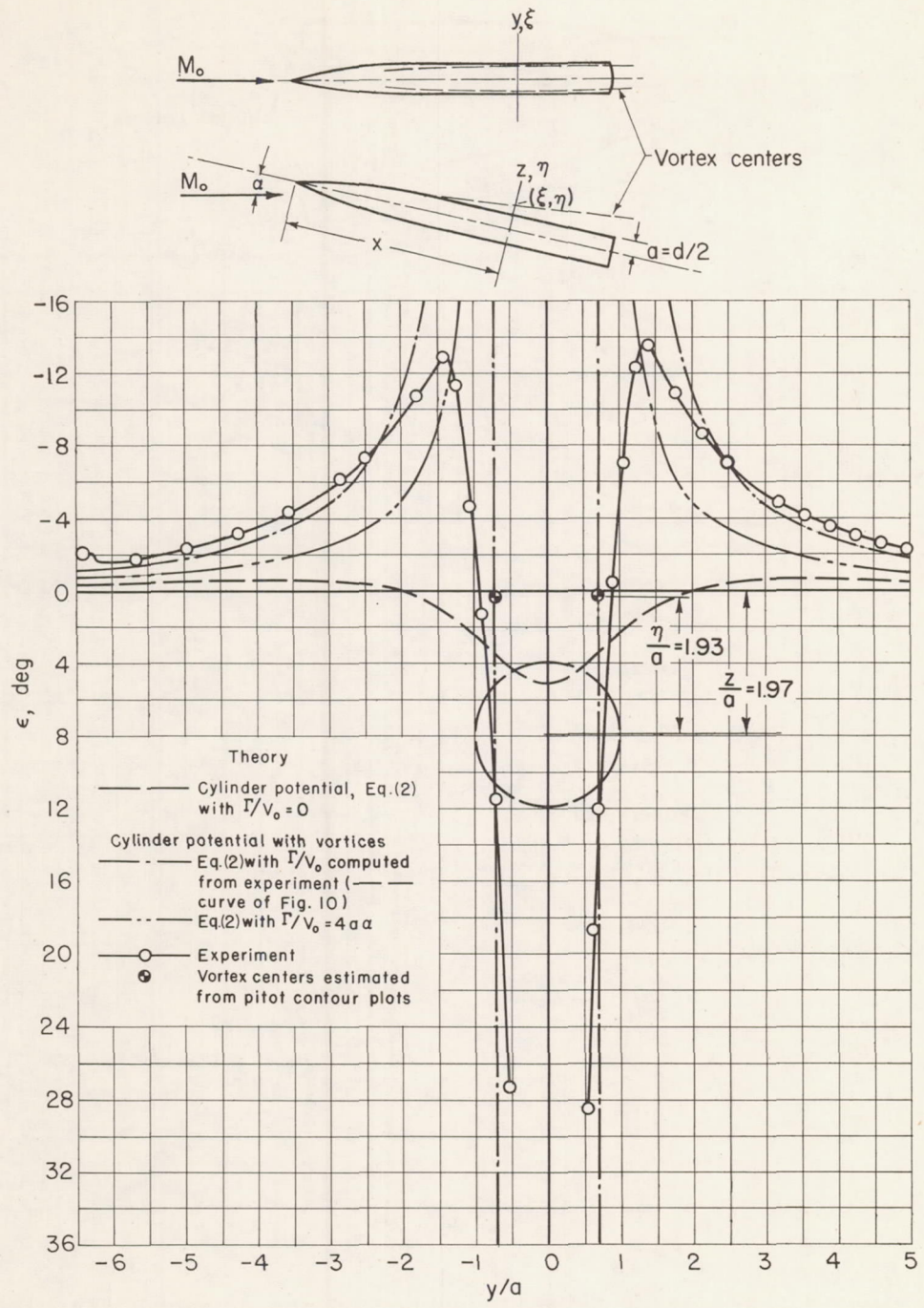
(e) $\alpha = 20^{\circ}$, $x/d = 6.7$

Figure 12.- Continued.



(f) $\alpha = 20^{\circ}$, $x/d = 8.5$

Figure 12.- Continued.



(g) $\alpha = 20^{\circ}$, $x/d = 10.2$

Figure 12.- Concluded.

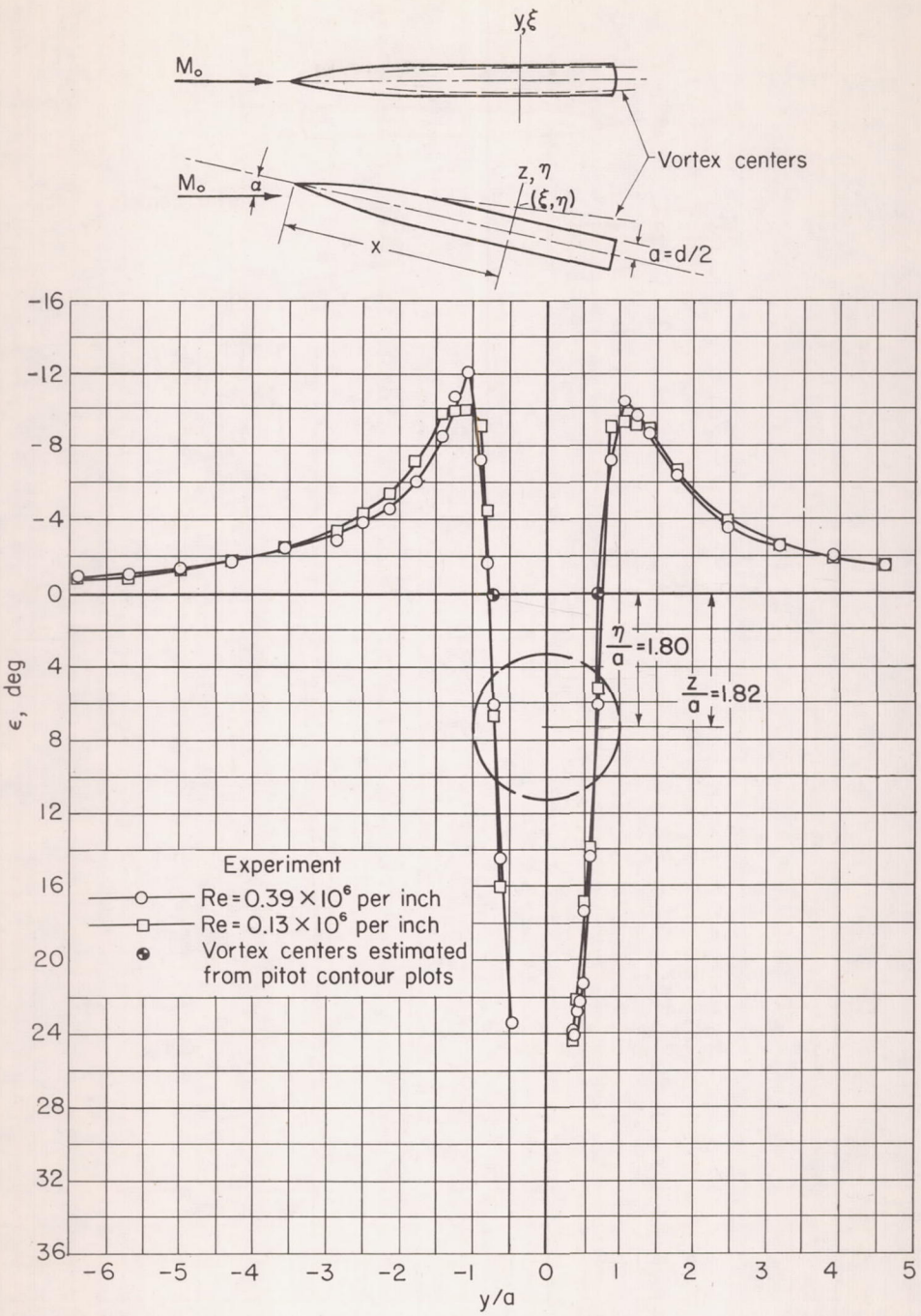


Figure 13.- Effect of Reynolds number on the downwash distributions through the body vortices for $\alpha = 15^{\circ}$ and $x/d = 10.2$; $M_0 = 1.98$.

NACA - Langley Field, Va.